



**HAL**  
open science

# Subsurface Structure at the InSight Landing Site From Compliance Measurements by Seismic and Meteorological Experiments

B Kenda, M Drilleau, R Garcia, T Kawamura, N Murdoch, N Compaire, P Lognonné, A Spiga, R Widmer-schmidrig, P Delage, et al.

► **To cite this version:**

B Kenda, M Drilleau, R Garcia, T Kawamura, N Murdoch, et al.. Subsurface Structure at the InSight Landing Site From Compliance Measurements by Seismic and Meteorological Experiments. *Journal of Geophysical Research. Planets*, 2020, 125 (6), pp.e2020JE006387. 10.1029/2020je006387 . hal-03657932

**HAL Id: hal-03657932**

**<https://u-paris.hal.science/hal-03657932>**

Submitted on 3 May 2022

**HAL** is a multi-disciplinary open access archive for the deposit and dissemination of scientific research documents, whether they are published or not. The documents may come from teaching and research institutions in France or abroad, or from public or private research centers.

L'archive ouverte pluridisciplinaire **HAL**, est destinée au dépôt et à la diffusion de documents scientifiques de niveau recherche, publiés ou non, émanant des établissements d'enseignement et de recherche français ou étrangers, des laboratoires publics ou privés.

# JGR Planets

## RESEARCH ARTICLE

10.1029/2020JE006387

### Special Section:

InSight at Mars

#### Key Points:

- Ground compliance measurements by InSight depend on the elastic properties in the near surface of Mars
- Observed compliance from convective vortex encounters and other pressure fluctuations opens the way to the exploration of the near surface
- Markov chain Monte Carlo inversion for the Young modulus profile suggests stratification within and below the regolith

#### Correspondence to:

B. Kenda,  
kenda@ipgp.fr

#### Citation:

Kenda, B., Drilleau, M., Garcia, R. F., Kawamura, T., Murdoch, N., Compaire, N., et al. (2020). Subsurface structure at the InSight landing site from compliance measurements by seismic and meteorological experiments. *Journal of Geophysical Research: Planets*, 125, e2020JE006387. <https://doi.org/10.1029/2020JE006387>

Received 29 JAN 2020

Accepted 14 APR 2020

Accepted article online 17 APR 2020

## Subsurface Structure at the InSight Landing Site From Compliance Measurements by Seismic and Meteorological Experiments

B. Kenda<sup>1</sup>, M. Drilleau<sup>1</sup>, R. F. Garcia<sup>2</sup>, T. Kawamura<sup>1</sup>, N. Murdoch<sup>2</sup>, N. Compaire<sup>2</sup>, P. Lognonné<sup>1</sup>, A. Spiga<sup>3,4</sup>, R. Widmer-Schmidrig<sup>5</sup>, P. Delage<sup>6</sup>, V. Ansan<sup>7</sup>, C. Vrettos<sup>8</sup>, S. Rodriguez<sup>1</sup>, W. B. Banerdt<sup>9</sup>, D. Banfield<sup>10</sup>, D. Antonangeli<sup>11</sup>, U. Christensen<sup>12</sup>, D. Mimoun<sup>2</sup>, A. Mocquet<sup>7</sup>, and T. Spohn<sup>13</sup>

<sup>1</sup>Université de Paris, Institut de physique du globe de Paris, CNRS, Paris, France, <sup>2</sup>Institut Supérieur de l'Aéronautique et de l'Espace ISAE-SUPAERO, Toulouse, France, <sup>3</sup>Laboratoire de Météorologie Dynamique / Institut Pierre-Simon Laplace (LMD/IPSL), Sorbonne Université, Centre National de la Recherche Scientifique (CNRS), École Polytechnique, École Normale Supérieure (ENS), Paris, France, <sup>4</sup>Institut Universitaire de France (IUF), Paris, France, <sup>5</sup>Black Forest Observatory, Stuttgart University, Wolfach, Germany, <sup>6</sup>Ecole des Ponts ParisTech, Laboratoire Navier/CERMES, Marne la Vallée, France, <sup>7</sup>Laboratoire de Planétologie et Géodynamique, UMR6112-CNRS, Univ. Nantes, Univ. Angers, Nantes, France, <sup>8</sup>Division of Soil Mechanics and Foundation Engineering, Technical University of Kaiserslautern, Kaiserslautern, Germany, <sup>9</sup>Jet Propulsion Laboratory, California Institute of Technology, Pasadena, CA, USA, <sup>10</sup>Cornell Center for Astrophysics and Planetary Science, Cornell University, Ithaca, NY, USA, <sup>11</sup>Sorbonne Université, Muséum National d'Histoire Naturelle, UMR CNRS 7590, Institut de Minéralogie, de Physique des Matériaux et de Cosmochimie, IMPMC, Paris, France, <sup>12</sup>Max Planck Institute for Solar System Research, Göttingen, Germany, <sup>13</sup>German Aerospace Center (DLR), Institute of Planetary Research, Berlin, Germany

**Abstract** Measurements of ground compliance at the InSight landing site—describing the surface response to pressure loading—are obtained from seismic and meteorological data. Compliance observations show an increase with frequency indicating the presence of a stiffer rock layer beneath the exposed regolith. We performed a Markov chain Monte Carlo inversion to investigate the vertical profile of the elastic parameters down to 20 m below InSight. Compliance was inverted both freely and assuming prior knowledge of compaction in the regolith, and the limitations and strengths of the methods were assessed on the basis of theoretical considerations and synthetic tests. The inverted Young modulus exhibits an increase by a factor of 10–100 over the first 10–15 m, compatible with a structural discontinuity between 0.7 and 7 m. The proposed scheme can be used for joint inversion of other seismic, geological, or mechanical constraints to refine the resulting vertical section.

**Plain Language Summary** Pressure fluctuations of the Mars' atmosphere induce tiny deformations of the ground that can be measured by the very sensitive seismometer of the InSight mission. The amount of deformation depends on the elastic properties of the sandy regolith (the surface layer exposed and highly fractured by impacts) and of the underlying rocks and can thus be used to explore beneath the surface. In this work, we review the theory describing the ground motion caused by moving pressure perturbations, and we analyze the effect of various parameters (wind speed and layering in the subsurface). We then develop a method to retrieve a vertical profile of the elastic parameters beneath the lander from the measurements. After testing the method on ideal cases, we apply it to data from Mars: The results show that the regolith becomes stiffer with depth and that a layer of harder rock may be present below, with the interface possibly located between 0.7 and 7 depth. Determining the structure of the near surface provides constraints on the geologic history of the landing site and contributes to the explanation of measured seismic signals.

### 1. Introduction

The InSight (Interior Exploration using Seismic Investigations, Geodesy, and Heat Transport) mission landed on Mars on 26 November 2018. The main science goal of the mission is to probe the interior of Mars through seismic, geodetic, and heat-flow measurements: The relevant experiments are SEIS (Seismic

Experiment for the Interior Structure, Lognonné et al., 2019), RISE (Rotation and Interior Structure Experiment, Folkner et al., 2018), and HP3 (Heat Flow and Physical Properties Probe, Spohn et al., 2018), respectively. Additionally, the APSS package (Auxiliary Payload Sensor Suite, Banfield et al., 2018) ensures a continuous monitoring of the environment through atmospheric (pressure, air temperature, wind direction, and speed) and magnetic measurements.

The main rationale for including the APSS experiments in the InSight payload is to complement the seismic data with direct observations of the environment. Indeed, in addition to ground motion, a seismometer is sensitive to meteorological and magnetic fluctuations, either if installed at the surface (e.g., Lognonné & Mosser, 1993; Withers et al., 1996) or even in a seismic vault (Beauduin et al., 1996; Zürn & Widmer, 1995; Zürn & Wielandt, 2007). For the purposes of the SEIS experiment, it is thus necessary to monitor the environment, both to discriminate between seismic signals of internal or atmospheric origin (Spiga et al., 2018) and to decorrelate the pressure, wind, magnetic, and thermal signals from the seismic records in order to get a lower noise floor; see Mimoun et al. (2017) for a thorough discussion of the noise sources and Murdoch et al. (2017) and Garcia et al. (2020) for pressure decorrelation.

During the first 6 months of operations following the Wind and Thermal Shield (WTS) deployment, the InSight seismometers have shown this expected sensitivity to atmospheric phenomena, even during the 18:00–24:00 LMST when the wind generated signal is very small and wind is below the resolution of the wind sensors (Banfield et al., 2020; Lognonné et al., 2020). On Earth, seismic noise of environmental origin provides information both about the source of noise and the structure beneath the stations (see, e.g., Tanimoto et al., 2015). Although many techniques used in terrestrial studies, such as the extremely powerful micro-seismic noise tomography Shapiro and Campillo (2004), rely on seismic networks, a variety of methods work for single station and can thus be applied in the framework of InSight. These methods include the study of the long-period hum of the planet (Kobayashi & Nishida, 1998), developed in more detail for Mars by Nishikawa et al. (2019), the motion induced by oceanic or atmospheric pressure fluctuations (Crawford et al., 1991; Sorrells, 1971; Tanimoto & Wang, 2018), high-frequency resonances related to the very local structure (Bonney-Claudet et al., 2008; Nakamura, 1989), and seismic noise autocorrelations (Tibuleac & von Seggern, 2012).

Seismic sounding of the Martian subsurface has not been possible before the InSight mission, and the first results from Lognonné et al. (2020) and Banerdt et al. (2020) paved the way for more in-depth analysis, which is one of the goal of this paper. It is an important goal to confirm the nature of the Martian subsurface a couple meters or tens of meters deep from the surface, which thus far had only been indirectly derived from geological analysis (e.g., Golombek et al., 2017, 2018, for the InSight landing region) and to better assess the resolution of the compliance techniques in Mars's conditions. In this work, we focus on the ground deformation induced by propagating atmospheric pressure fluctuations: The reaction to the pressure loading depends on a property of the ground, the compliance. Indeed, the infinitesimal elastic strain of the ground under pressure forcing is governed by its mechanical compliance. The observed deformation at the surface is proportional to the amplitude of the pressure fluctuations and inversely proportional to the apparent stiffness of the ground. Similar work has been done on Earth with ocean bottom seismometers (Crawford et al., 1991) and data from the U.S. Transportable Array (Tanimoto & Wang, 2018), as well as with synthetic noise models for Mars and Earth (Kenda et al., 2017; Tanimoto & Wang, 2019). The goals of our work are thus (1) to analyze the compliance from combined seismic and pressure measurements, respectively, with the SEIS and APSS instruments; (2) to perform an inversion for the structure of the near surface layers at the InSight landing site; and (3) to discuss the resolution of the results and their consequences in terms of site geology.

This paper is organized as follows. In section 2, we recall the theoretical formulation describing the seismic signals induced by pressure fluctuations. In section 3, we present the data sets used in this study and two different techniques to retrieve the ground compliance from real data: The compliance is a byproduct of the pressure-decorrelation methods, discussed in more detail in a companion paper by Garcia et al. (2020). The resulting compliance profiles are shown, and the uncertainties and limitations were assessed. Section 4 is devoted to the Bayesian inversion of compliance profiles, from idealized synthetic cases to actual Mars data. Section 5 discusses the implications of these results for the stratigraphy at the InSight landing site.

**Table 1***Elastic Properties of Rock Units Expected in the Near Surface at the InSight Landing Site (Delage et al., 2017; Golombek et al., 2017; Morgan et al., 2018)*

Rock type	Young modulus (MPa)	Poisson's ratio	Ground velocity (m/s)*
Regolith (surface)	7.5	0.22	$1 \times 10^{-6}$
Regolith (1 m depth)	28	0.22	$3 \times 10^{-7}$
Coarse ejecta	520	0.24	$2 \times 10^{-8}$
Fractured bedrock	13,000	0.28	$7 \times 10^{-10}$
Basalt	65,000	0.25	$1 \times 10^{-10}$

*Note.* \* indicates the vertical seismic velocity induced by a 1 Pa pressure fluctuation and a background wind of 5 m/s if the seismometer was installed on a half space made of the respective unit.

Future developments and links to other observations constraining the near surface are briefly presented in the concluding section 6.

## 2. Theoretical Basis for Ground Compliance

Before detailing the theoretical aspects of the ground deformation induced by pressure fluctuations, it is worth providing some basic orders of magnitude: To infer them, one should keep in mind that the deformation observed at the surface depends both on the pressure loading and on the elastic properties in the near surface.

It is assumed that the InSight lander stands on a very degraded, impact crater of about 30 m in diameter, filled by aeolian material (sandy material), into Hesperian lava flows (Golombek et al., 2017, 2018, 2020). Based on geologic studies, the metric scale stratigraphy can be summed up in the following units: (1) sandy material with sparse pebbles down to at least 3 m in depth (Ansan et al., 2019; Golombek et al., 2020; Warner et al., 2019) corresponding to both regolith and aeolian material (we will refer to this unit simply as regolith); the fine-grained regolith grades into (2) coarse blocky ejecta; below, (3) fractured basalt corresponding to basaltic lava flow fractured by impactors, whose thickness is unknown; finally, (4) basaltic bedrock whose thickness is estimated to be about 200 m (Golombek et al., 2017). In Table 1, we list the relevant elastic properties for these units expected at the InSight landing site (Delage et al., 2017; Morgan et al., 2018). Our scope being to illustrate the order of magnitudes, we do not assess the uncertainties in the elastic properties. As detailed and justified below, the surface deformation induced by a moving pressure field over a homogeneous half space is characterized by a vertical velocity at the surface that is proportional to the amplitude of the pressure fluctuation and to the wind speed and inversely proportional to the Young modulus of the ground. Accordingly, Table 1 also shows the expected ground velocity for typical conditions on Mars (pressure fluctuation of 1 Pa and wind speed of 5 m/s).

The atmosphere of Mars is thin, and consequently, typical turbulent pressure fluctuations modeled (Spiga et al., 2018) and observed Banfield et al. (2020) at the InSight landing site range from a few tenths of a Pa to a few Pa (Spiga et al., 2018). Nevertheless, the presence of a regolith layer (Golombek et al., 2017) is responsible for relatively large surface deformations induced by those pressure loadings (as compared to stiff bedrock, see Table 1). These can be felt by a sensitive seismometer such as SEIS, which is able to measure tiny deformations inducing ground velocities of less than  $10^{-9}$  m/s at 10 s period (Lognonné et al., 2019). The pressure noise induced by a unit pressure fluctuation and a wind speed of 5 m/s (typical of near-surface Martian conditions) can be clearly detected based on the expected elastic properties in the near surface. Additionally, these values illustrate the effect of the seismometer installation on the background noise during the turbulent daytime.

To model the effect of a propagating pressure fluctuation over a realistic subsurface model, we proceed by steps describing (1) the effect of a static pressure load on a homogeneous elastic half space; (2) the effect of a propagating pressure load on a homogeneous elastic half space; and (3) the same effect over a one-dimensional horizontally layered model. Several other effects, such as the gravitational attraction of the moving air masses or the free-air anomaly (less than 5% of the signal for frequencies above 1 mHz on Mars), are present but not significant for our applications (Spiga et al., 2018; Zürn et al., 2007; Zürn & Wielandt, 2007).

InSight and HiRise observations (e.g., Banerdt et al., 2020) suggest that the wind is predominantly blowing along a stable direction during daytime. We are therefore assuming in what follows that the largest pressure gradient is along the wind direction, which we will note  $x$ . Synthetic tests made prior to launch on 3-D large eddies simulations have furthermore validated this hypothesis for compliance analysis (e.g., Kenda et al., 2017).

In case (1), the pressure field exerted by the atmosphere at the surface is therefore assumed to depend on the wind direction horizontal coordinate only, say  $x$ :

$$P = P(x) = \int_{k_x} P(k_x) e^{ik_x x} dk_x, \quad (1)$$

where  $k_x$  is the wave number. For every Fourier component, the displacement  $u$  at the surface can be derived from the elasto-static equation with the pressure field giving the boundary condition for vertical stress (see e.g., Sorrells, 1971) in terms of the elastic properties of the half space:

$$u_z(k_x) = -\frac{2}{k_x} \frac{1-\nu^2}{E} P(k_x), \quad (2)$$

$$u_x(k_x) = \frac{i}{k_x} \frac{(1+\nu)(1-2\nu)}{E} P(k_x). \quad (3)$$

Here,  $E$  denotes the Young modulus and  $\nu$  the Poisson's ratio of the homogeneous half space, and the  $z$  axis points upwards.

In order to model a propagating pressure fluctuation  $P = P(x, t)$ ,  $t$  being the time coordinate, we follow Sorrells hypothesis (Sorrells, 1971) and assume that the fluctuation is advected by an ambient wind with speed  $c$  parallel along the  $x$ -axis, that is,

$$P(x, t) = P(x - ct). \quad (4)$$

This implies that the wave number of the fluctuation satisfies  $k_x = \omega/c$ , where  $\omega$  is angular frequency. This formulation gives the elastic response to pressure loading in the frequency domain, with the resulting formulas:

$$v_z(\omega) = -2ic \frac{1-\nu^2}{E} P(\omega), \quad (5)$$

$$v_x(\omega) = c \frac{(1+\nu)(1-2\nu)}{E} P(\omega). \quad (6)$$

Here,  $v$  indicates ground velocity, and we refer to  $v_z$  and  $v_x$  as *inertial* velocities, since they are related to a true motion of the ground. In addition to these inertial motions, the ground deformation induces a tilt angle in the  $x$  direction:

$$\theta_x = \frac{\partial u_z}{\partial x} = ik_x u_z = -2i \frac{1-\nu^2}{E} P(k_x). \quad (7)$$

For small angles  $\theta_x$ , this tilt induces the acceleration felt by the seismometer is

$$a_{\text{tilt},x} = g \sin \theta_x \sim g \theta_x, \quad (8)$$

where  $g = 3.71 \text{ m/s}^2$  is surface gravity. This last term induces the apparent horizontal velocity

$$v_{x,\text{tilt}}(\omega) = \frac{2}{\omega} g \frac{1-\nu^2}{E} P(\omega). \quad (9)$$

The absolute value of the ratio between the resulting ground velocity  $v$  and the pressure  $P$  is called *compliance*. To be more specific and avoid confusion between the compliances that can be defined with equations (5) and (6), we define the vertical and horizontal compliance  $\kappa_v, \kappa_h$  as

$$\kappa_v = 2c \frac{1-\nu^2}{E}, \quad \kappa_h = c \frac{(1+\nu)(1-2\nu)}{E}. \quad (10)$$

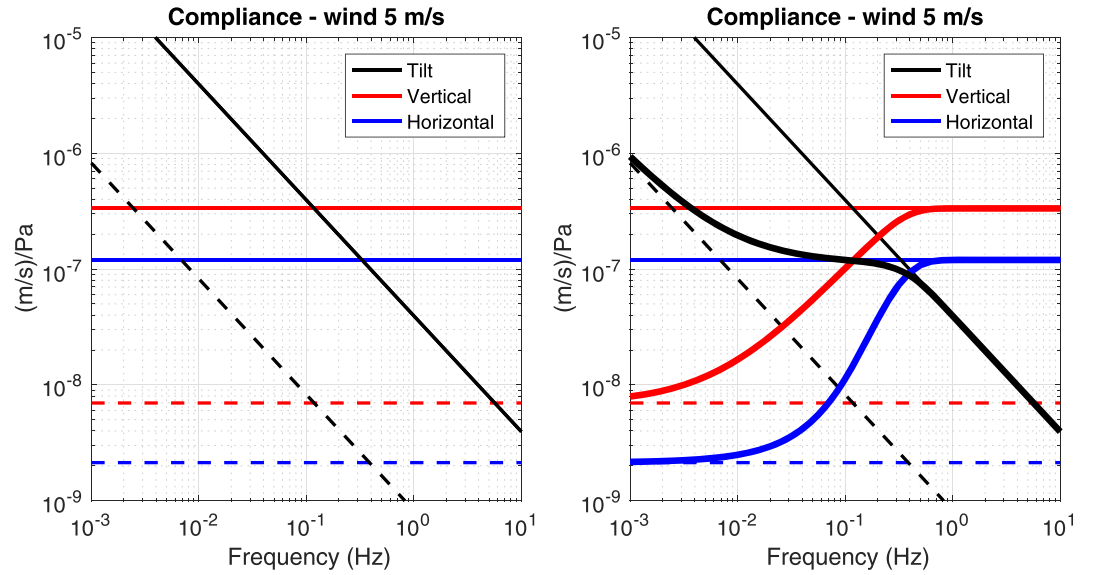


**Figure 1.** Compliance for different ground structures. Left panel: the three main effects (horizontal tilt, horizontal inertial, and vertical inertial) are shown for two different homogeneous half spaces, namely, regolith and coarse ejecta (continuous and dashed lines, respectively). Right panel: Compliance for a two-layered model consisting of a 5 m thick regolith over a coarse ejecta half space. The compliance for the layered model is represented by the thick continuous lines. Note that at high frequency, it converges to the compliance for the regolith half space (thin continuous lines) and at long period to the substrate compliance (dashed lines).

The *normalized compliance* is obtained by dividing by the wind speed  $c$ :

$$\bar{\kappa}_v = \kappa_v/c, \quad \bar{\kappa}_h = \kappa_h/c. \quad (11)$$

Tilt is related to normalized vertical compliance through the equation

$$\bar{\kappa}_v = \frac{\omega V_{x,tilt}}{g P}. \quad (12)$$

For a homogeneous half space, normalized compliance depends only on the elastic properties; therefore, it is more suitable to investigate the subsurface structure.

From this theoretical formulation, it follows that (1) the inertial vertical effect is larger than the horizontal one by a factor  $V_p^2/V_s^2$ ,  $V_p$  and  $V_s$  being the  $P$  and  $S$  wave velocities, respectively; (2) the tilt effect increases with period, whereas the inertial effect is flat in velocity (that is, frequency independent); (3) the inertial effects become larger with increasing wind speed, as opposed to the tilt effect. In relation to this last point, the critical frequencies above which the vertical response is larger than tilt ( $f_{c,v}$ ) and above which the horizontal signal is larger than tilt ( $f_{c,h}$ ) can be derived by comparing equations (5) and (6):

$$f_{c,v} = \frac{g}{2\pi c}, \quad f_{c,h} = \frac{g}{2\pi c} \frac{V_p^2}{V_s^2}. \quad (13)$$

This is illustrated in Figure 1 for two different media (regolith at 1 m depth and coarse ejecta, see Table 1)

In the case of a horizontally layered half space, no simple formula relating the ground motion to the pressure forcing (the equivalent of equations (5) and (6) for the homogeneous half space) is available. The solution to the elastostatic equation can however be obtained with a Thomson-Haskell propagator method (Haskell, 1953; Sorrells et al., 1971; Thomson, 1950). In this case, the compliance becomes frequency dependent: If we assume a single layer lying over a homogeneous half space (Figure 1), it can be seen that at high frequencies, the properties of the top layer dominate, whereas at long periods, the half space properties become relevant.

We now explore the effect of the various parameters involved in a simple case: We consider a two-layered model with fixed elastic parameters in the first layer and vary those parameters and the depth of the

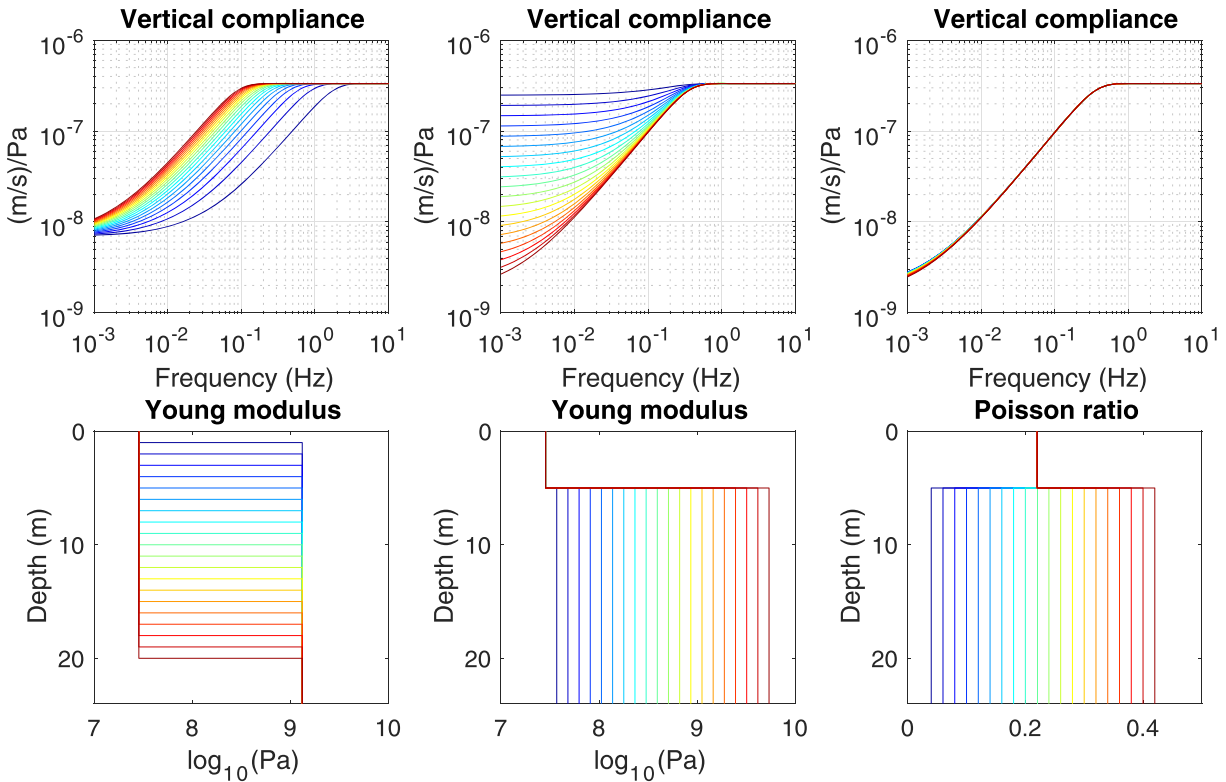


**Figure 2.** Sensitivity of vertical ground compliance to various parameters for a two-layered model. The top row shows the vertical compliance for a wind speed of 5 m/s for the models shown in the bottom row. From left to right, the depth of the second layer, the Young modulus, and the Poisson's ratio in the second layer are varied.

discontinuity in the second layer (Figure 2). We conclude that (1) increasing the depth of the second layer shifts the compliance profile towards lower frequencies; (2) increasing  $E$  of the second layer lowers the compliance values at long and intermediate periods; and (3) varying  $\nu$  does not significantly affect the results.

Another way to look at the relationship between subsurface structure, frequency, and observed compliance is through sensitivity kernels, as done by, for example, Doran and Laske (2019) and Zha and Webb (2016) for seafloor compliance and by Tanimoto and Wang (2019) for surface seismometers. Considering for simplicity  $E$  only, its sensitivity kernel  $S$  is defined by the integral equation

$$\frac{\delta \bar{\kappa}_v}{\bar{\kappa}_v} = \int_{-\infty}^0 S(z) \frac{\delta E}{E} dz, \quad (14)$$

where  $\delta$  indicates a perturbation of the reference model and compliance (Tanimoto & Wang, 2019). An example of the sensitivity kernel for a Mars subsurface model is shown in Figure 3: The results for different frequencies correspond to different penetration depths of the pressure-induced fluctuation, which compare with terrestrial results by Tanimoto and Wang (2019). As pointed out by Doran and Laske (2019), however, the sensitivity kernels are extremely dependent on the reference model, and therefore, we did not use them further in our inversion scheme.

Another key parameter is the mean wind speed, for which the situation is slightly more complicated. Indeed, increasing the wind speed has two competing effect: First, the inertial effect (on both the vertical and horizontal components) scales like the wind speed, whereas ground tilt does not depend explicitly upon wind. Second, the wavelength of the pressure fluctuation is proportional to the wind speed; thus, for a given frequency, the sensitivity depth (that is, the region determining the compliance observation at the surface) increases with the wind speed. This is shown in Figure 4: For ground tilt, only the sensitivity depth depends on the wind; therefore, for a given frequency (and increasing stiffness with depth), the compliance decreases when wind increases. For the inertial effect, the behavior is more complex, but, generally speaking, stronger

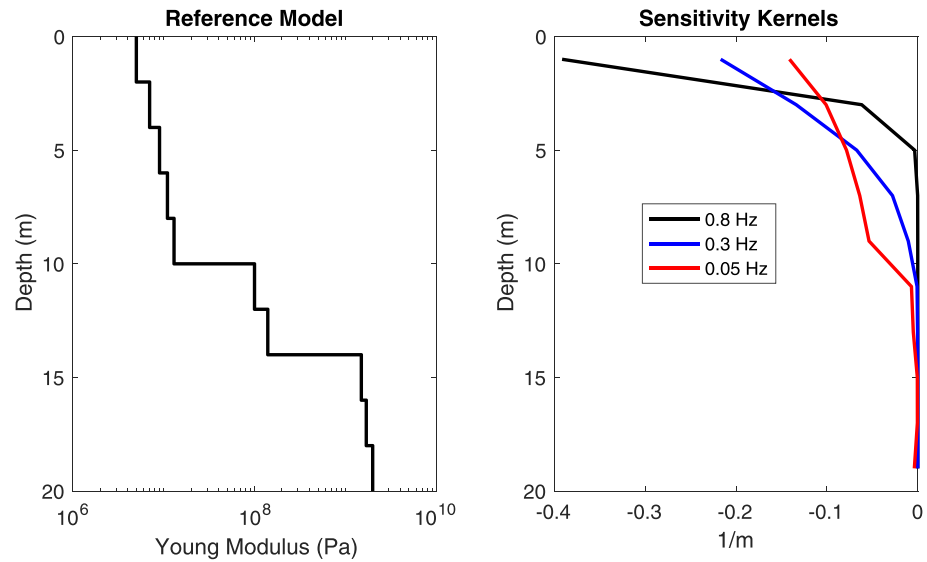


**Figure 3.** Depth sensitivity kernels for the Young modulus. The reference model to be perturbed is shown on the left panel ( $\nu$  is fixed to 0.25 in all layers). The sensitivity kernels are shown for three different frequencies, and it is clear that at high frequencies the sensitivity to the structure is limited to shallow depth. The computation were done for a wind speed of 5 m/s.

winds imply larger pressure noise, although the relationship is frequency dependent and nonlinear. These results show that, apart from the simple case of a homogeneous half space, when inferring the subsurface structure from compliance measurements (derived from vertical or tilt seismic signals), it is necessary to take into account the wind speed. Furthermore, analyzing ideal synthetic cases, Kenda et al. (2017) and Murdoch et al. (2017) showed that the tilt effect is sensitive to the pressure field over a larger area. Therefore, when a single pressure sensor is available, estimates derived from the vertical component may be more reliable than tilt-derived estimates. Reconstruction of the trajectory of the pressure fluctuations is instead needed when evaluating compliance from ground tilt. Additionally, since the horizontal components are sensitive to both tilt and ground motion produced by pressure loading, it may be challenging to correctly separate the two effects. For these reasons, in the rest of this work, we focused on the compliance observed from the vertical component.

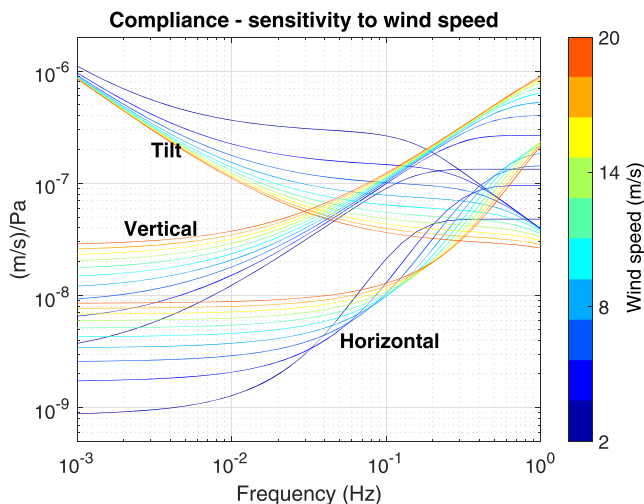


**Figure 4.** Sensitivity of ground compliance to wind speed for a two-layered model. The color scale corresponds to the wind speed. The values for wind speed have been chosen as typical for the InSight landing site given the observed wind speeds by APSS.

### 2.1. The Effect of Compaction and Confining Stress in the Regolith Layer

The theory discussed above can now be applied to the geologic context of the InSight landing site to enlighten another key aspect. Pre- and post-landing geological studies (Ansan et al., 2019; Golombek et al., 2017, 2020; Warner et al., 2019) indicate the presence of a layer of sandy regolith, estimated to be between 3 and 11 m thick based on the analysis of rocky ejecta craters (Warner et al., 2017). Beneath the regolith, stiffer layers of coarse ejecta and fractured bedrock are present. The mechanical properties of the regolith were studied making use of laboratory experiments with Martian simulants (Delage et al., 2017) and theoretical considerations (Morgan et al., 2018). The resulting pre-landing model has of course large uncertainties (e.g., the actual thickness of the regolith layer or the density values of the surface layer); however, it clearly shows that we cannot assume that the regolith layer has homogeneous elastic properties. Indeed, even neglecting compaction, the elastic properties (for our purposes, the Young modulus) strongly depend upon the confining stress, hence upon depth (Morgan et al., 2018). This dependence is illustrated in Figure 5: The reference model by Morgan et al. (2018) is shown

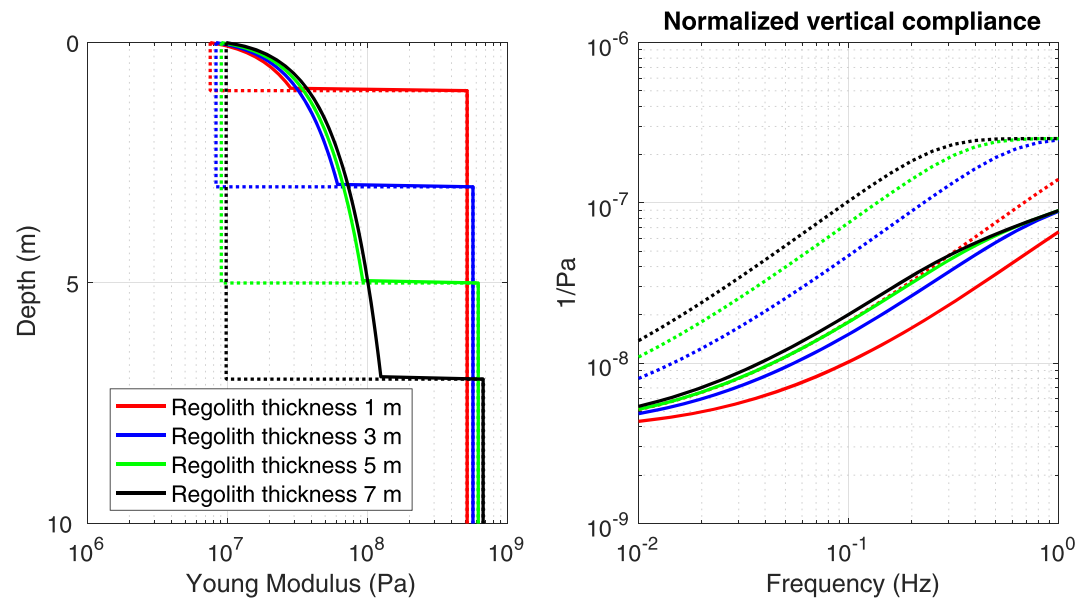


**Figure 5.** Compliance for the pre-landing model by Morgan et al. (2018) for different thicknesses of the regolith layer (in different colors, see legend). The left panel shows the realistic models (continuous lines) together with simple models assuming homogeneous properties within the regolith layer (dashed lines). The different models are slightly shifted for illustration purposes. The corresponding profiles of normalized vertical compliance ( $\bar{\kappa}_v$ ) are shown on the right panel: note the large difference between realistic and simple models, as well as the small effect of the regolith thickness once the effect of the confining stress on  $E$  is taken into account.

for different thicknesses of the regolith and compared to the corresponding homogeneous models. It can be seen that  $E$  increases by a factor 4 over the first meter and by an order of magnitude at 5 m depth.

For this set of models, we computed the normalized compliance as described above (by densely discretizing the vertical profile of  $E$  every 5 cm in order to mimic the effect of a continuous increase). The compliance profiles exhibit a large difference between simple models (that is, with a homogeneous regolith layer) and models accounting for the effects of confining stress (Figure 5). Furthermore, once the confining stress is considered, the effect of different regolith thickness is mitigated, and therefore, it becomes difficult to infer this parameter. This point is extremely important for the inversion strategy and for the interpretation of inversion results.

### 3. Compliance Observations at the InSight Landing Site

#### 3.1. Dataset for This Study

InSight landed on 26 November 2018 at Elysium Planitia, and the SEIS experiment was deployed on the ground on Sol 22 and covered with the Wind and Thermal Shield on Sol 66 (Banerdt et al., 2020; Lognonné et al., 2020). Since Sol 73, the SEIS seismometers have been functioning in the nominal mode of operation producing an almost continuous high-quality dataset (Lognonné et al., 2020). SEIS includes two three-axis seismometers, the VBB (very broad band) and SP (short period) fully described in Lognonné et al. (2019). In this study, we focused on the VBB data since these sensors have better performances in the frequency range of our interest, which is below 1 Hz. The VBBs produce two different datastreams: the VEL and POS outputs (proportional to ground velocity and acceleration, respectively). The preprocessing of seismic data includes standard procedures (removal of the transfer function to retrieve ground motion in physical units, axis recombination to the standard geographical frame Vertical/North/East). The geographic north with respect to the SEIS reference frame was determined through a sundial (Savoie et al., 2019). The APSS experiment did not require a deployment and monitored the atmospheric and magnetic environment almost continuously since the beginning of operations. The meteorological channels used in this work are limited to calibrated pressure and wind data (Banfield et al., 2020). We analyzed data from Sol 73 to Sol 227, all of which are publicly available (InSight Mars SEIS data Service, 2020).

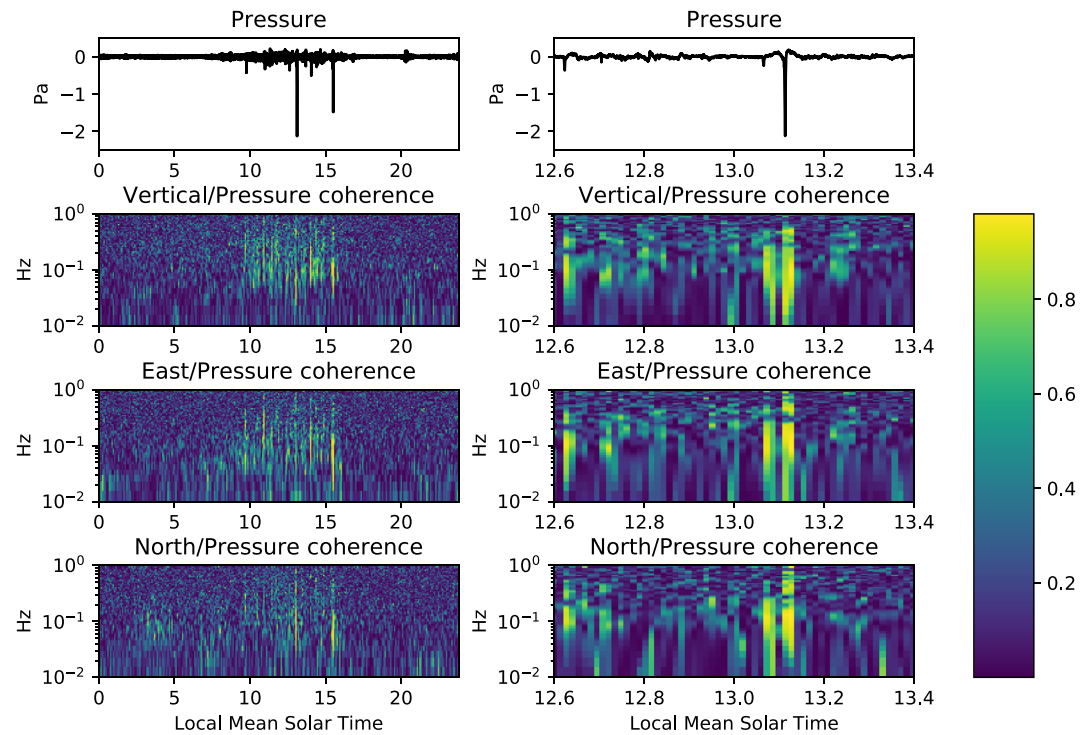


**Figure 6.** Coherence between the pressure and very broad band (VBB) seismic signals over Sol 114. The pressure time series are high-pass filtered at 600 s. Coherence ranges from 0 (blue) to 1 (yellow). It appears that the coherence is high mostly for short time windows corresponding to strong pressure signals, for example, convective vortices during the daytime. The right panels are a zoom into 12.5–13.5 local time.

To ensure that the comparison of seismic and pressure data gives access to the ground compliance as described in section 2, it is necessary to check whether the seismic signals are actually generated by the pressure fluctuations (Murdoch et al., 2017). An efficient way to do it is to measure the coherence between the time series and hence measure the amount of the power spectral density of the seismic signal that is explained by pressure variations. This is shown in Figure 6 for Sol 114 through a coherogram, illustrating how coherence varies with local time for the three seismic axes. It can be seen that the background coherence level is low during the nighttime, and it increases during the daytime when convective turbulence in the planetary boundary layer is strong (Banfield et al., 2020; Spiga et al., 2018). However, zooming in in the daytime shows that high coherence is mostly limited to the occurrence of strong pressure signals, mainly pressure drops that indicate encounters with convective vortices (dust devils, if enough dust particles are carried within the vortex). The coherograms of Figure 6 show that the high coherence (say, above 0.8) between pressure and seismic time series required for compliance analysis is generally limited to the band 0.02–0.9 Hz. We will thus focus on this limited range, although episodes with high coherence at higher (or lower) frequency are possible and can be individually studied. For a more complete analysis of the coherence and the observed effects of pressure fluctuations, we refer to the companion paper by Garcia et al. (2020).

### 3.2. Measurements From Dust Devil Convective Vortices

Since they often exhibit a large coherence between pressure and seismic signals, convective vortices are well suited to perform compliance measurements (Kenda et al., 2017). We considered about 360 vortices encountered between Sol 73 and Sol 169. From the whole catalog of pressure drops larger than 0.25 Pa, we selected (in an almost-automated procedure, including a final manual quality check) a subset of events (i) that had a large coherence and (ii) whose vertical seismic signal could be simply modeled with a single proportionality coefficient based on the theory of section 2. In particular, we considered vortex encounters for which the coherence between seismic and pressure time series have a coherence larger than 0.5. The procedure, described in more details in Garcia et al. (2020) and Lognonné et al. (2020), gives—for each event—a measurement of the apparent compliance in a certain frequency range (determined by requiring a reduction both of the coherence with pressure and of the spectral density of the seismic signal). By taking

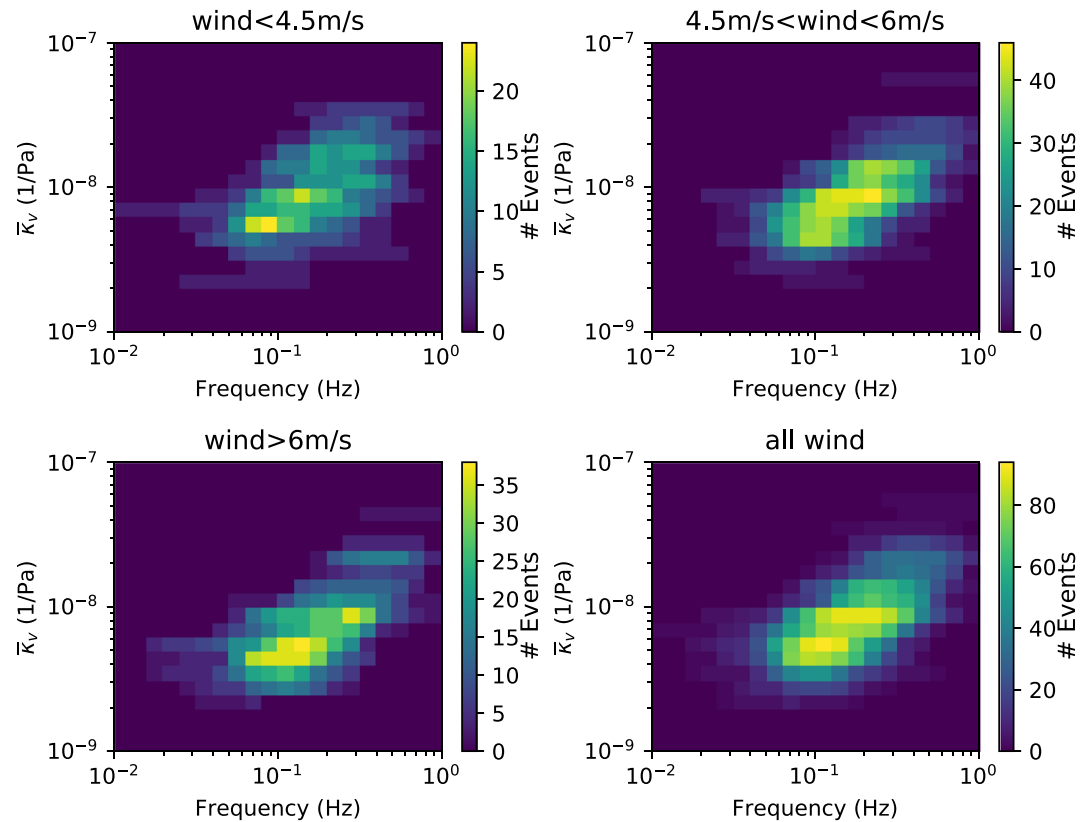


**Figure 7.** Distribution of normalized vertical compliance ( $\bar{\kappa}_v$ ) derived from dust devil convective vortices as a function of frequency. The color scale corresponds to the number of events, and the different panels are for various ambient wind conditions.

as ambient wind speed the average value over 1 min before and after the vortex encounter (removing the vortex encounter itself), we derive the normalized compliance (Figure 7).

Based on the discussion in section 2, and in particular on the effect of the ambient wind on the apparent normalized compliance for layered media, one could claim that it is not possible to derive statistics from events occurring in different wind conditions. However, clustering of the resulting compliance measurements based on the wind speed does not show significantly different results (Figure 7). This means that the variance of the compliance values alone, taken here as a measure of the uncertainty, dominates over the effect of wind speed when enough events are considered. Therefore, we decided to consider the whole compliance distribution regardless of wind speed (and to use the observed wind distribution in the inversion scheme, as described later). Notice that this distribution has a clear trend, namely, an increase of compliance with frequency, in agreement with a *normal* layering in the subsurface, that is, an increase of stiffness (or Young modulus) with depth.

### 3.3. Measurements From Compliance Marker

A pressure decorrelation method has been implemented by using adaptive least mean square (LMS) algorithm with a step-size reduction mechanism (Garcia et al., 2020; Kwong & Johnston, 1992). This algorithm optimizes an acausal finite impulse response (FIR) filter between pressure and SEIS velocity components in an adaptive way. If the pressure noise dominates SEIS signals, the compliance is simply the FIR filter response. However, as described by Garcia et al. (2020), the FIR filter response is biased by other noise sources and possible correlations between pressure and other noise drivers such as wind speed. As a consequence, we decided not to use these compliance estimates that are generally biased towards lower values.

Instead, another method similar to the one described in the previous section has been implemented to estimate compliance values. This automated method is described in Garcia et al. (2020). It is based on a marker

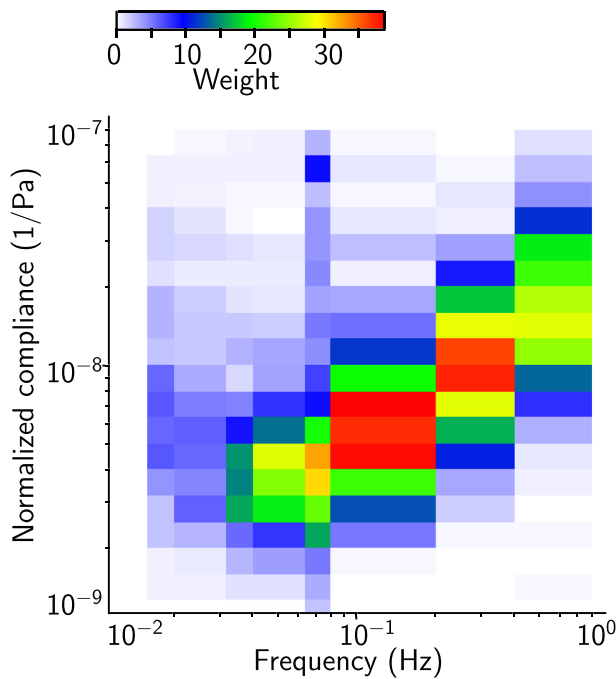


**Figure 8.** Normalized vertical compliance ( $\bar{\kappa}_v$ ) measurements from VEL and POS channels using the compliance marker, shown as a pdf with the color scale.

of compliance events which is using the phase relations between pressure and SEIS components. Band-pass filtered records (in the  $[f_1, f_2]$  Hz range) of pressure ( $P$ ), vertical velocity ( $V_z$ ), and horizontal velocity along the wind direction ( $V_h$ ) are used to implement a compliance marker defined by

$$I_G(t) = \frac{STA(P^2)}{LTA(P^2)} CC_T(P, Hil(V_z)) CC_T(P, V_h) CC_T(Hil(V_z), V_h), \quad (15)$$

where  $Hil(V_z)$  is the Hilbert transform of vertical velocity record, the  $STA()$  and  $LTA()$  functions stand, respectively, for short-term average performed on the time interval  $[t - T/2, t + T/2]$  and long-term average performed on  $[t - 20T/2, t + 20T/2]$ , and the  $CC_T(X, Y)$  function stands for correlation coefficient between  $X$  and  $Y$  for the time range  $[t - T/2, t + T/2]$ .  $T$  is defined by  $T = \frac{3}{f_1}$ . The last three terms of the equation should be equal to one if in the time range  $[t - T/2, t + T/2]$ ,  $P$ ,  $Hil(V_z)$ , and  $V_h$  are perfectly correlated, as expected from compliance relation. The first term is an amplitude ratio ensuring that the pressure variations are above background noise. Then, a threshold value is set (typically 0.3 or 0.4) above which the event is considered and the vertical and horizontal compliances are estimated. Finally, in order to ensure that the signal is also above noise on SEIS components, only events with  $\frac{STA(|V_z|)}{LTA(|V_z|)} > 2$  are selected. Figure 8 shows the resulting distribution of the normalized compliance obtained from the vertical component based on both VEL and POS seismometer outputs. The normalized compliance values compare well with the measurements from dust devil convective vortices (Figure 7), obtained in a fully independent way.

#### 4. Inversion: From Compliance to Near-Surface Structure

The inverse problem consists in retrieving the elastic properties (Young modulus and Poisson's ratio) in the near surface as a function of depth from the compliance measurements. This problem is, however, ill-posed: Different subsurface models can give similar compliance values, at least in the frequency band of our interest. This is shown in Figure 9: The compliance for four models, which were selected only for illustration and have different  $E$  profiles (and  $\nu$  fixed to 0.25 for simplicity), is shown. The four models are clearly distinguishable if the whole frequency band 0.001–10 Hz is considered, whereas, if the observation is limited to the 0.02–0.3 Hz band, their compliance agrees within a factor of 2 (note that  $E$  can vary, at a fixed depth, by more than two orders of magnitudes among the models!).

Moreover, even with a full bandwidth observation, not all the models can be distinguished through compliance observations (indeed, it is the case for two of the models, which share similar Young moduli but present a large difference in the depth of the major discontinuity). For subsequent interpretation, it is also useful to note that a thin soft layer at the surface (red model in Figure 9, 0.5 m thick) has little or no effect in the bandwidth of our interest (below 1 Hz), even if it affects higher frequencies. Moreover, thin layers at depth, even with large contrasts in elastic properties (green model in Figure 9), have little impact on the smooth compliance curve.

Due to the ill-posed nature of the problem, inversions based on least squares or grid search in the absence of regularization cannot be expected to retrieve the ground structure, nor to estimate the uncertainties. Recently, a method based on depth sensitivity kernels was proposed by Tanimoto and Wang (2019); however, its convergence may depend strongly on the choice of the starting model. Instead, we used a Bayesian approach based on the Markov chain Monte Carlo (MCMC) method: The probabilistic inversion is more suitable to explore the parameter space, include a priori information, provides reliable estimates of the uncertainties, and is fully independent from the starting model.

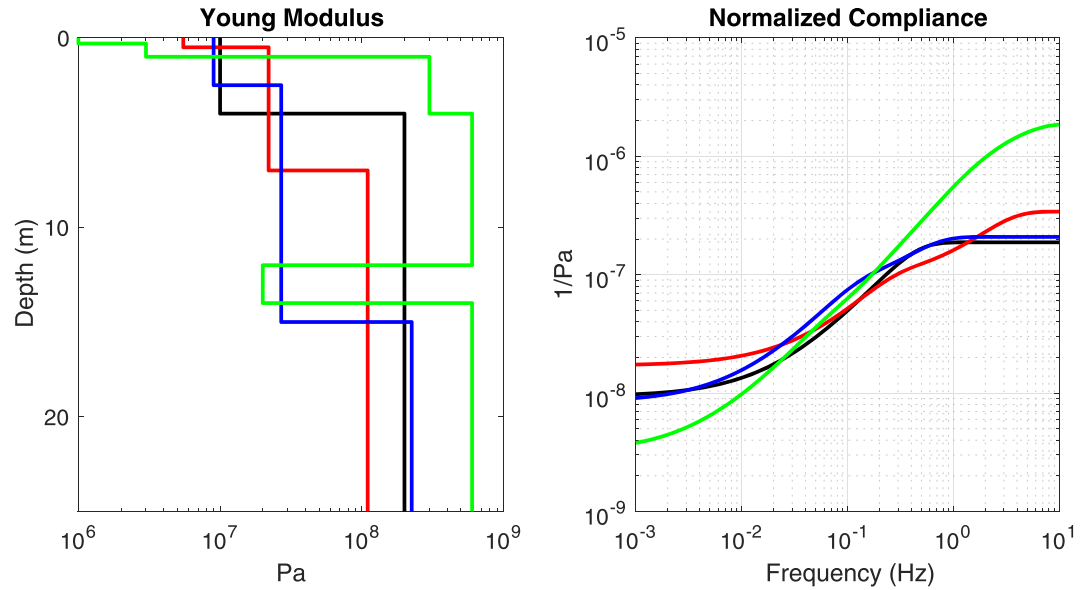


**Figure 9.** Example of different subsurface models (left panel) having similar  $\bar{\kappa}_v$  compliance values (right panel) in the band 0.02–0.3 Hz. Note that despite a large difference in the depth of the major discontinuity, the black and blue models have close compliance values over the full bandwidth. For all models  $\nu$  is fixed to 0.25.

#### 4.1. Inverse Problem

##### 4.1.1. MCMC Algorithm

An MCMC algorithm is used to sample solutions (i.e., physical configurations) of the inverse problem that fit the observations within data uncertainties. The solutions are sampled according to a set of rules named priors, which define the set of possible models reducing the configuration space and representing our state of knowledge. We employ the probabilistic procedure developed by Drilleau et al. (2013) and used in Panning et al. (2015, 2017) and Lognonné et al. (2020).

This section briefly outlines the fundamentals of the Bayesian inversion, based on the MCMC method, detailed in Mosegaard and Tarantola (1995) and Mosegaard (1998). Bayesian approaches allow to go beyond the classical computation of the unique best-fitting model by providing a quantitative probabilistic measure of the model resolution, uncertainties, and non-unicity. In a Bayesian framework, the known prior information on the parameters is combined with the observed data to generate the a posteriori distribution of the model parameters. MCMC methods perform a nonlinear guided search by sampling the parameter space according to the posterior probabilities. After a “burn-in” period, which is necessary to loose the memory of the initial configuration (starting model), MCMC methods perform a nonlinear guided search by sampling the parameter space according to the posterior probabilities.

Let us denote by  $\mathbf{p}$  the parameters of our model and  $\mathbf{d}$  the data, respectively. The data are related to the parameters through the equation,  $\mathbf{d} = A(\mathbf{p})$ , where the non-analytic and nonlinear operator  $A$  represents the forward problem discussed in section 2. Explicitly, the parameters are the depths, the Young modulus, and Poisson’s ratio of each layer. In the Bayesian framework, a set of parameters is randomly chosen at each iteration. The corresponding  $E$  and  $\nu$  profiles are then used to compute the compliance as a function of frequency. The solutions of the inverse problem are described by the posterior probabilities  $P(\mathbf{p}|\mathbf{d})$  that the parameters are in a configuration  $\mathbf{p}$  given the data are in a configuration  $\mathbf{d}$ . The parameter space is sampled according to  $P(\mathbf{p}|\mathbf{d})$ . Bayes’ theorem links the prior distribution  $P(\mathbf{p})$  and the posterior distribution  $P(\mathbf{p}|\mathbf{d})$ ,

$$P(\mathbf{p}|\mathbf{d}) = \frac{P(\mathbf{d}|\mathbf{p})P(\mathbf{p})}{\sum_{\mathbf{p} \in \mathcal{M}} P(\mathbf{d}|\mathbf{p})P(\mathbf{p})}, \quad (16)$$

where  $\mathcal{M}$  denotes all the configurations in the parameter space.  $P(\mathbf{p})$  defines the prior distribution, that is, the set of possible models which reduce the configuration space and represents our state of knowledge.

**Table 2**  
*Synthesis of the Inverted Parameters and the Prior Bounds Considered for M1 and M2 Models*

Parameter	Lower bound	Upper bound
M1 model		
Layers' depth (m)	0	20
Young Modulus (Pa)	$10^6$	$10^{11}$
Poisson's ratio	0.05	0.45
M2 model		
Young modulus at the surface (Pa)	$5 \cdot 10^5$	$10^8$
Poisson's ratio at the surface	0.1	0.333
$\beta$	0.2	0.3
Regolith thickness (m)	0	20
Young modulus below the regolith (Pa)	$10^6$	$10^{11}$
Poisson's ratio below the regolith	0.05	0.45

The probability distribution  $P(\mathbf{d}|\mathbf{p})$  is a function of the misfit  $S(\mathbf{d}, A(\mathbf{p}))$ , which determines the difference between the observed data  $\mathbf{d}$  and the computed synthetic data  $A(\mathbf{p})$ . The input compliances as a function of frequency data are provided in the form of 2-D matrices (Figures 7 and 8), which give a weight to each (frequency, compliance) couple. In practice, each time a new model is randomly sampled, a weight is given for each frequency according to compliance value in the 2-D matrix. The sum of the weights for all the frequencies gives the misfit value. To estimate the posterior distribution (equation (16)), we employ the Metropolis algorithm (Hastings, 1970; Metropolis et al., 1953), which samples the model space with a sampling density proportional to the unknown posterior probability density function. This algorithm relies on a randomized decision rule which accepts or rejects the proposed model according to its fit to the data and the prior.

#### 4.1.2. Model Parameterization and A Priori Conditions

The Bayesian formulation enables a priori knowledge to be accounted for. We choose to compare two different parameterizations, one with relatively few a priori conditions on the Young modulus and Poisson's ratio (called M1) and another one using physical assumptions (called M2). Table 2 summarizes the inverted parameters and the prior bounds considered for M1 and M2 models. It is worth noting that these parameterizations cover a range that is larger than the realistic properties of the expected rocks; however, this does not affect the inversion results and guarantees instead the robustness of the inversion scheme. Indeed, considering a large parameter space for the inverse problem ensures that no physically acceptable region may be missed because of boundary effects.

The first set of models is parameterized using several layers of variable thicknesses (a good compromise turned out to be eight layers, apart for a synthetic test where we used two layers only). The varying parameters are the depth of each layer,  $E$  and  $\nu$  for each considered layer. The parameters are randomly sampled in relatively wide parameter spaces (Table 2), with no assumption on the depth of the structural discontinuities.

A second set of models is parameterized considering physical assumptions in the regolith. The model is divided into two parts: the regolith and an underlying geological unit (expected, but not requested, to be stiffer). This unit could be made of coarse ejecta, fractured bedrock, or basaltic lava flows, or a combination of those, but due to limited resolution, we do not attempt to extract information about further layering. In the regolith, we consider that the medium is densely compacted, using the empirical law from Morgan et al. (2018).  $E$  and  $\nu$  at the surface are randomly sampled during the inversion scheme, within the ranges detailed in Table 2. Equations 1 and 20 from Morgan et al. (2018) are then used to compute the whole  $E$  and  $\nu$  profile as a function of depth within the regolith layer. The uncertainty on this compaction model is taken into account by varying the experimentally determined and nondimensional exponent  $\beta$  of equation 20 from Morgan et al. (2018). This  $\beta$  parameter describes the exponential increase of the elastic parameters with confining stress. The thickness of the regolith layer is randomly sampled between 0 and 20 m. Below the regolith, a single homogeneous unit is assumed, whose Young modulus and Poisson's ratio can vary within the same range of values as for the M1 models.

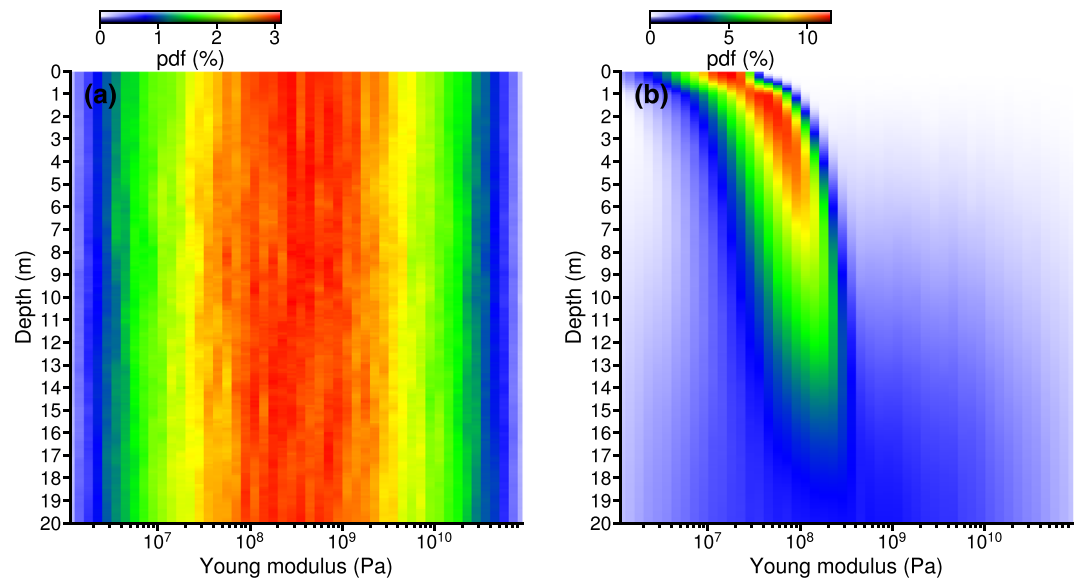


**Figure 10.** Probability density functions of the Young modulus for M1 (a) and M2 models (b), considering that all the sampled models which are in good agreement with a priori information detailed in Table 2 are accepted. These are the priors of the M1 and M2 inversions detailed below. Eight layers are considered in M1 models. Red and blue colors show high and low probabilities, respectively. Although the color map is the same, the corresponding absolute probability values differ from (a) to (b). The prior probability density function (pdf) is computed by counting the number of sampled profiles in each of the cases. The discretization for  $E$  is log-constant (with an incremental step of  $10^{0.1}$ , whereas the discretization for depth is constant [0.1 m]). For a given depth, the sum of the pdf over all the parameter intervals is equal to 100%.

Figures 10a and 10b show the prior distributions of  $E$  profiles of M1 and M2 models, respectively, assuming the conditions detailed in Table 2. Both the a priori assumptions and the sampling of the models lead to nonuniform distributions. Concerning M1 models (Figure 10a), the pdf does not vary significantly with depth, but the center of the parameter space is better sampled than the bounds. In the MCMC algorithms, new models are proposed by randomly perturbing the previously accepted model. Here, the sampling of the parameter space is performed using a continuous proposal function. Defining the  $t$ th and the  $(t + 1)$ th value of a parameter  $p$ , as  $p^t$  and  $p^{t+1}$ , respectively, then the subsequent step may be defined as  $p_i^{t+1} = p_i^t + w^i$ , where  $w^i$  is the  $t$ th stepsize, randomly sampled from a normal distribution with zero mean. A Gaussian probability density distribution, centered at  $p_i^t$ , is classically used to randomly sample the  $p_i^{t+1}$ , which explains why for a given depth, the pdf decreases when moving away from the center of the parameter space. Contrary to the M1 pdf (Figure 10a), the a priori distribution of M2 models (Figure 10b) is strongly depth-dependent, because compaction and confining stress are accounted for in the regolith (Morgan et al., 2018). The pdf is spread as a function of depth, because of the homogeneous layer below the regolith. As for the M1 pdf, the bounds of the distribution are less sampled. Note that we verified the efficiency of the inversion process and the sampling by realizing several synthetic tests with extreme values of the parameters space as input. The tested models were retrieved with success by the algorithm. We stress that no covariance structure is imposed to the prior. This choice was made to avoid including prior information in this first study and to explore all possible structural models. However, this choice makes very rough models possible, which can be excluded by imposing a more informed prior covariance structure. Future inversions may benefit of this alternative approach.

#### 4.2. Synthetic Tests

In order to assess the efficiency of the inversion scheme described above and to understand its limitations, we performed synthetic tests in idealized cases. More precisely, we considered a simple 1-D model consisting of two horizontal layers, computed the theoretical compliance, and added noise to the resulting frequency-dependent compliance to mimic the kind of distributions we get from real data (section 3). The wind speed is fixed to 5 m/s. Two cases are considered: (1) frequency band for compliance limited from 0.04 Hz to 0.7 Hz and (2) full frequency band 0.01–1 Hz. All these tests are conducted using the first set of models (M1).

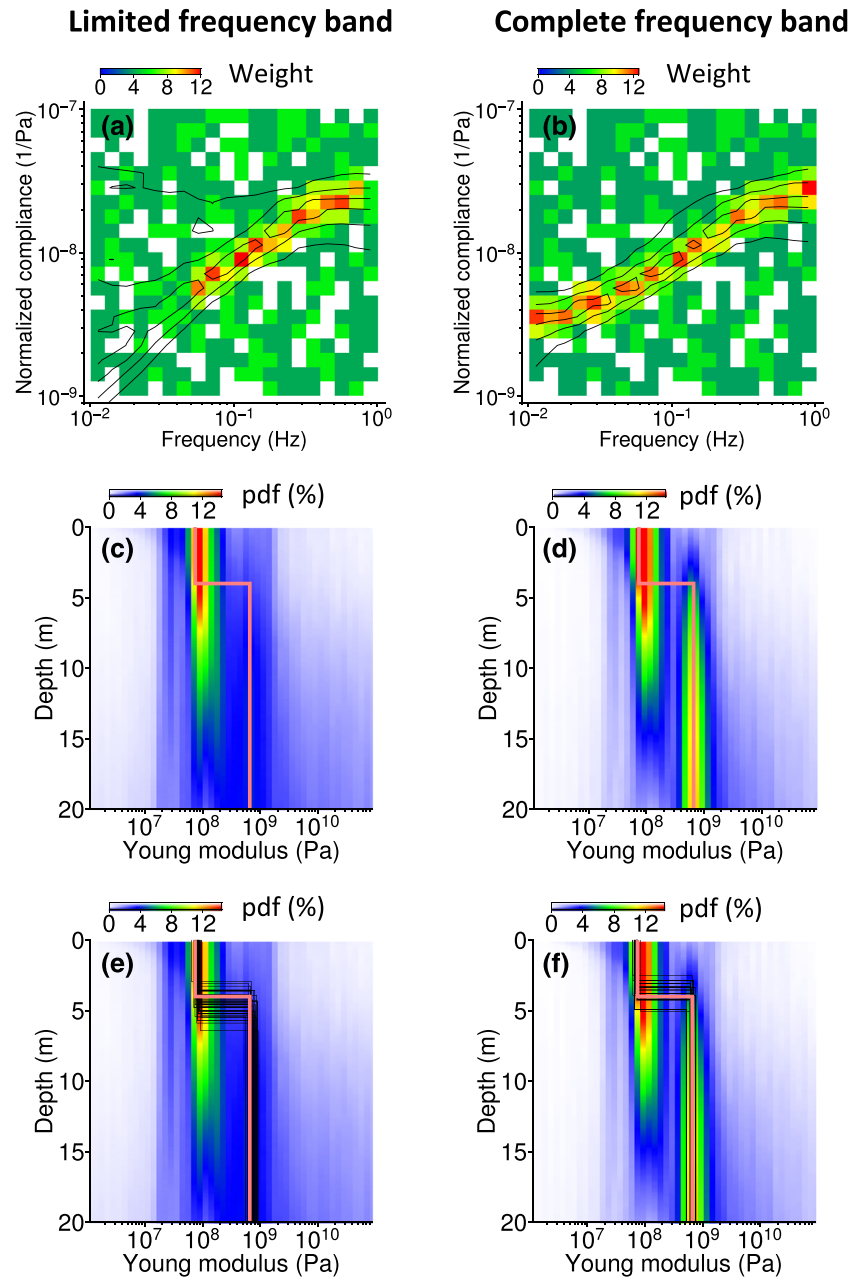


**Figure 11.** Compliance inversion results for a two-layered structure in the synthetic case using model M1. (a) The input normalized compliance with noise added is shown as a pdf with the color scale; the output compliance is represented through contour lines enclosing 30%, 60%, and 90% of the data. (c) pdf of the retrieved Young modulus as a function of depth (color scale), and the input model (orange continuous line); blue and red colors show low and high probabilities, respectively. (e) same as (c), but with the 50 best models overplotted. (b), (d), and (f) same as (a), (c), and (e) but for the full-bandwidth inversion.

In order to fully characterize the results, a first inversion was made for exactly the same kind of input model, that is, by inverting for a structure consisting of just two horizontal layers. This will allow the marginal probabilities of the various parameters to be evaluated and compared to the true value. The input and output distributions are shown in Figure 11, together with the corresponding  $E$  profiles compared to the true one. In both cases, we observe that the Young modulus of the first layer is correctly retrieved: Indeed, the output pdfs show high probability in the vicinity of the true input model (Figures 11c and 11d). In return,  $E$  of the second layer is only constrained using the full frequency band.  $\nu$  is, however, not constrained and is therefore not shown. In this ideal case, the results can be better appreciated by analyzing three free parameters

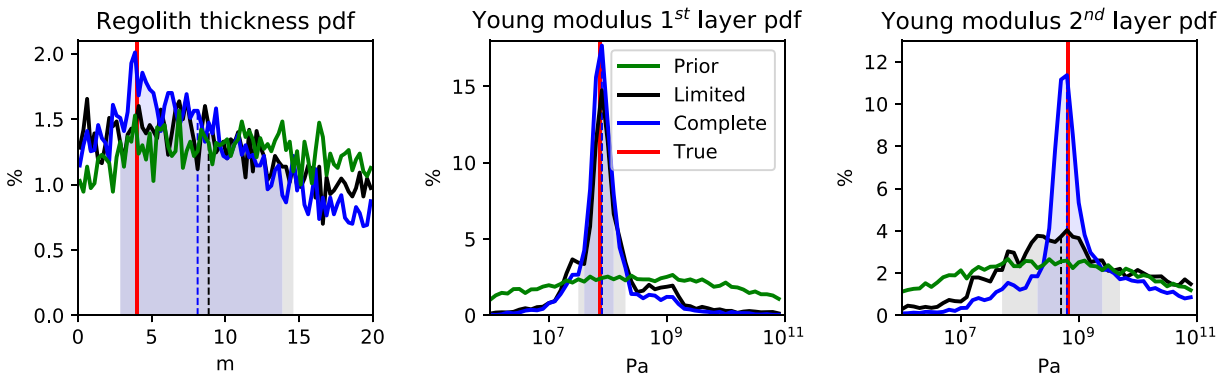


**Figure 12.** Performance of the inversion scheme on the synthetic tests. The three relevant parameters of model M1 are shown from left to right: the thickness of the first layer, its Young modulus, and the Young modulus in the second layer. The prior distribution is shown in green, the true value in red, whereas the probability distributions from the limited- and full-bandwidth inversions are shown in black and blue, respectively. The shaded area denote the 1-sigma intervals centered on the median values (dashed lines).

independently, namely, the thickness of the first layer and  $E$  in the two layers, whose marginal probabilities are shown in Figure 12. It can be noted that  $E$  in the first layer is well estimated in both the full and limited bandwidth case, whereas to retrieve  $E$  of the second layer, knowledge of the full bandwidth compliance is necessary. The thickness of the first layer is, however, not as well constrained as the Young modulus. Nevertheless, analysis of the fit suggests that the right thickness can be inferred by maximizing the fit, as suggested by the best-fit models shown in Figures 11e and 11f, which cluster around the true thickness of 4 m. A more careful analysis of the fit as a function of thickness (Figure 13) confirms this interpretation. In the limited bandwidth case, however, the fit for thicknesses of about 4 m is, in a statistical sense, not better as compared to the one for other values. For the full bandwidth case, instead, the fit distribution is significantly better for thickness values close to the true one.

An additional inversion test on the same dataset was made by relaxing the assumption on the number of layers, increasing it to 8 at random depths (recall that the input model had only two layers). The inversion results are shown in Figure 14. As expected, the resolution at intermediate depth is in this case worse (since thin layers with arbitrary Young moduli can be inserted without significantly affecting the compliance profile), but  $E$  in the first layer is correctly retrieved and interestingly its thickness as well. Indeed, although it is not immediately clear how to define a discontinuity from pdfs, it appears that resolution is good down to

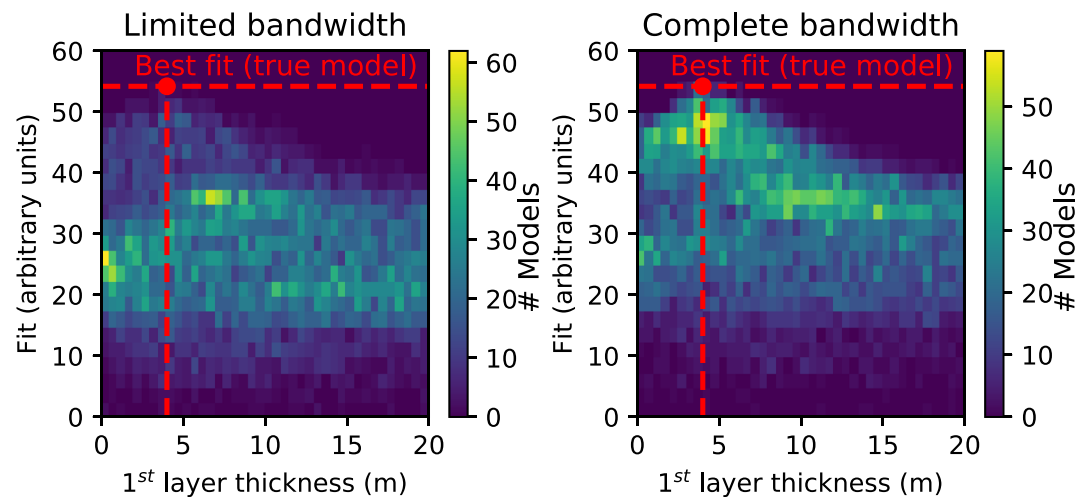


**Figure 13.** Fit of the output models M1 as a function of the thickness of the first layer. For each sampled model, the fit to data is defined by the sum of the weights of the cells intersected by its compliance curve (Figure 11). The color scale gives the frequency distribution in terms of number of sampled models. The left panel is for the limited-bandwidth inversion, the right panel for the complete bandwidth inversion. The red lines indicate the best theoretical fit and the true value for the thickness of the first layer.

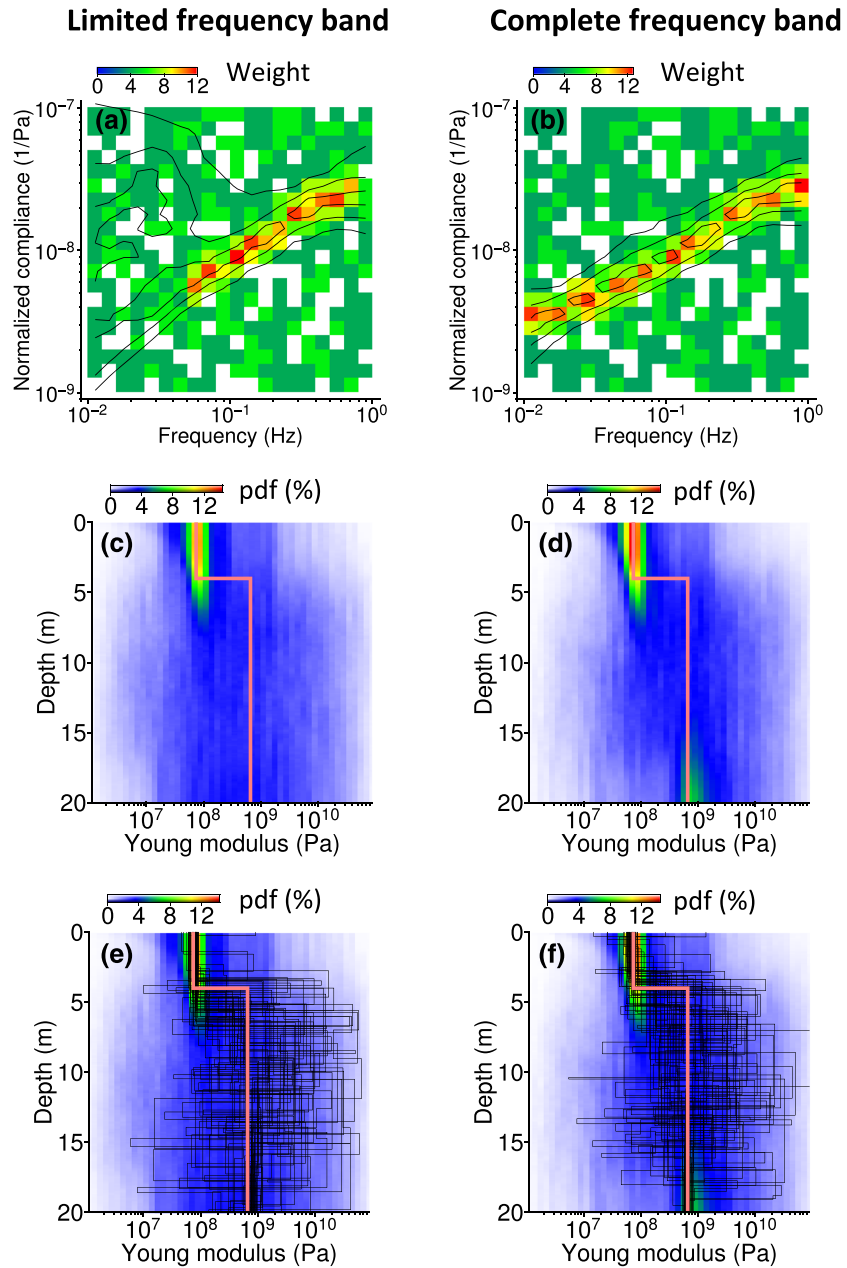


**Figure 14.** Same as Figure 11, but here, the number of layers in the inversion scheme is increased to 8.

about 4 m, which is the true thickness of the first layer. Moreover, in the full-bandwidth case (Figures 14b and 14d),  $E$  towards 20 m (and below) is correctly retrieved. Note that having better resolution below a certain depth is related to the inversion scheme, since fixing a half-space structure for the lowermost layer triggers the convergence of the models towards the true value of  $E$ . At intermediate depths, instead, small layers with almost arbitrary values of  $E$  can be inserted, producing a less constrained distribution.

### 4.3. Inversion of Mars Data

#### 4.3.1. Inversion Assuming a Layered Structure

The first inversion performed on ground compliance observed by InSight (section 3) was done without assuming a priori knowledge of the Martian near surface from geology and geotechnical experiments. Hence, we considered the M1 model class (Table 2) and assumed a horizontally layered structure (eight layers) over a homogeneous half space. In all inversions of Martian data, the wind speed was chosen in the distribution observed for the corresponding data set.

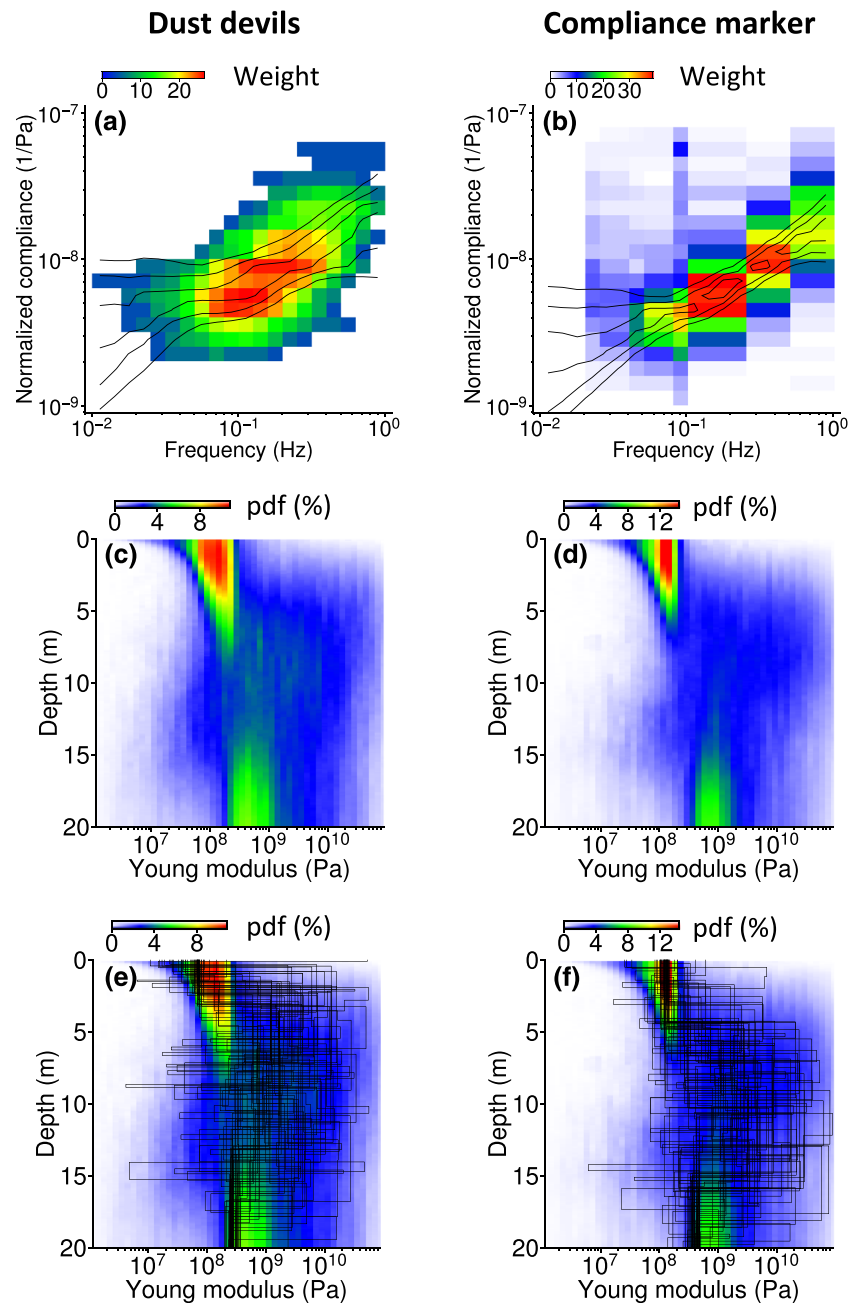


**Figure 15.** Inversion of compliance observed at the InSight landing site with dust devil convective vortices and the compliance marker. (a) and (b) show the pdf of the measurement (color scale) together with the posterior compliance distribution given by contours of 0.3, 0.6, and 0.9 probability. (c) and (d) show the distribution of the retrieved Young modulus with depth. (e) and (f) additionally show the 50 best fitting models (black lines). The corresponding prior distribution of  $E$  with depth is shown in Figure 10a.

The results are presented in Figure 15. First of all, it should be noticed that the inversion scheme is able to reproduce the observed distributions of compliance with frequency (Figures 15a and 15b). Moreover, as both measurement techniques exhibit a trend of compliance with frequency, the retrieved vertical profiles of  $E$  are characterized by an increase of stiffness with depth (Figures 15c and 15d), suggesting the presence of a major discontinuity between 3 and 15 m depth (see section 5 for an interpretation of these results). In addition to this, the distribution is relatively well constrained close to the surface and below 15 m depth, whereas at intermediate depths the acceptable values for  $E$  are spread. This was also the case for the synthetic test described above (Figure 14d) and inherently depends on the possibility of adding thin layers with arbitrary

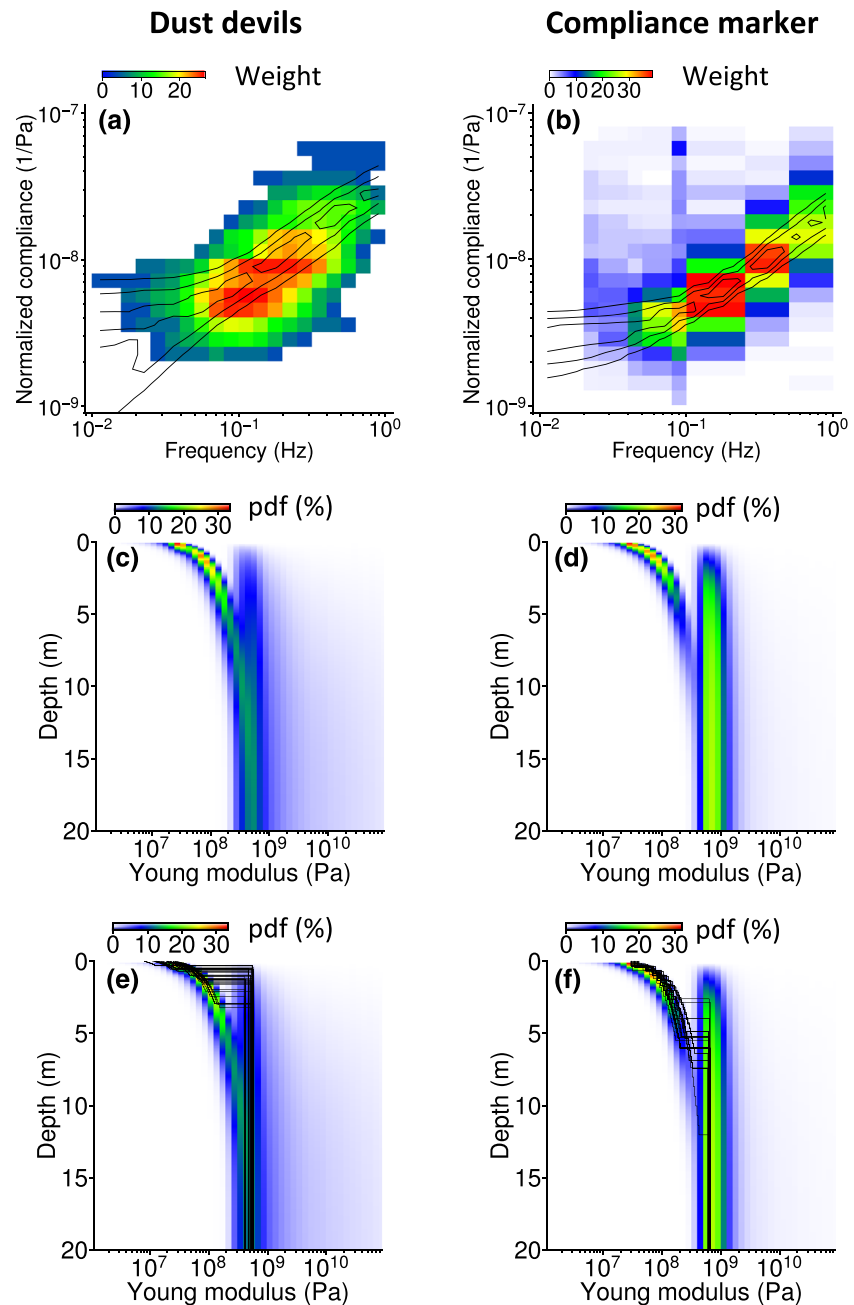


**Figure 16.** Same as Figure 15 but assuming a compaction profile and the effect of confining stress on the elastic parameters in the regolith layer (see Table 2 and Figure 10b for the prior distribution).

elastic parameters at intermediate depths without affecting the compliance profile (Figure 9). Indeed, where a half space structure is imposed, the models have no more the freedom to include layers with little effect on the observed compliance and, accordingly, cluster towards Young modulus values that fit the data.

#### 4.3.2. Inversion Assuming a Compaction Profile

A second inversion assumed a compaction profile in the regolith as well as the effect of confining stress on  $E$  as described in section 4.1.2 (M2 model class). In this case, the general behavior of the retrieved Young modulus (Figures 16c and 16d) is similar for the inversion based on dust devil vortex events and compliance marker. Note however that the increase of the Young modulus in the regolith layer (corresponding to the continuously bend region close to the surface) is strongly determined from the prior assumptions (Figure 10b). Nevertheless, a comparison with the prior distribution suggests a relatively thin regolith layer,

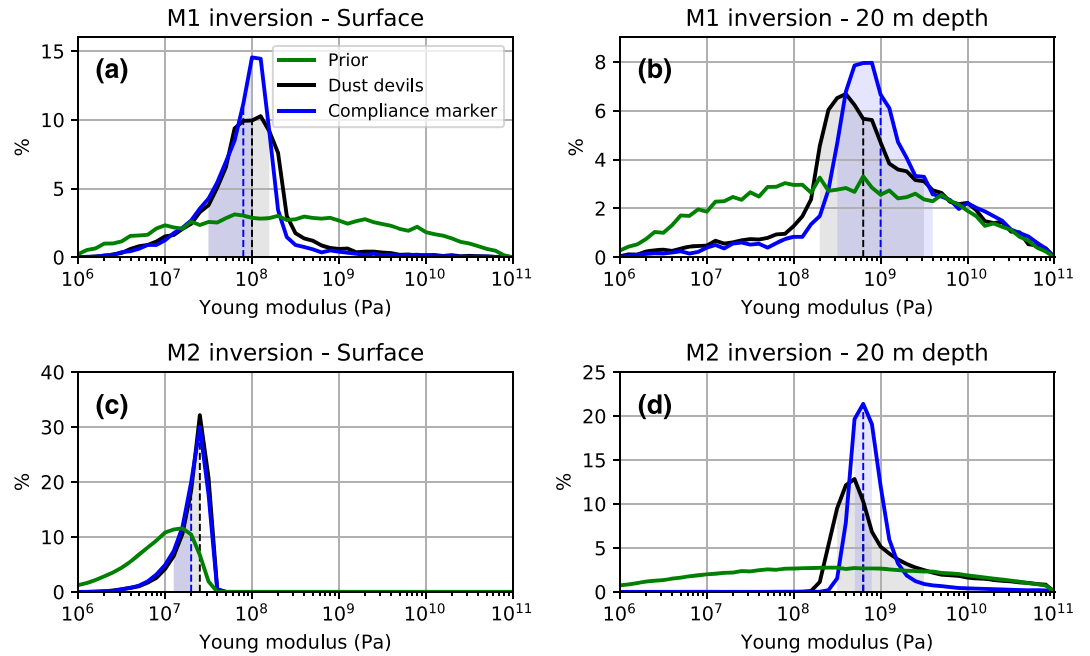


**Figure 17.** Young modulus pdfs at fixed depths. (a) is for the M1 inversion at the surface; (b) for the M1 inversion at 20 m depth; (c) for the M2 inversion at the surface; (d) for the M2 inversion at 20 m depth. In each plot, the prior distribution is shown in green, the results for the dust devil inversion in black, and the results for the compliance marker inversion in blue. The dashed lines indicate the median value and the shaded areas the  $1\sigma$  confidence intervals. Note that the compliance marker inversion has generally less spread distributions.

and a Young modulus below the regolith layer constrained by the inversion procedure. It is also worth noting that  $E$  below the regolith layer is similar to those found in the inversion without a priori. These points, together with the general interpretation of the results, will be further discussed in section 5.

## 5. Discussion

In order to avoid overinterpretation or misinterpretation of the inversion results presented in section 4.3, we critically review here those results and their implications in terms of the near-surface structure at the InSight landing site. To do it, we analyze some key parameters summarizing the outputs of the inversions (the Young modulus at the very surface and at depth and the regolith thickness) and compare them with pre-landing expectations.

First of all, we consider the Young modulus at the very surface as retrieved from the two proposed inversion schemes (Figures 17a and 17c). The pre-launch proposed Young modulus at the surface is 7.5 MPa (Morgan et al., 2018, Table 1), increased to about 20 MPa beneath the SEIS feet due to the weight of the sensor assembly. The inversions considering a layered structure give the  $1\sigma$  confidence intervals of 30–200 MPa for the dust devil vortices dataset and 30–125 MPa for the compliance marker inversion (Table 3). Assuming a density of  $1,300 \text{ kg/m}^3$  and  $\nu = 0.25$ , we express these ranges by using the expression of the  $P$  wave velocity:  $V_p = \frac{(1-\nu)E}{\rho(1+\nu)(1-2\nu)}$ . This provides ranges of 166–430 and 166–340 m/s, respectively. These values are significantly higher than both the pre-launch one and those measured by the HP<sup>3</sup> travel times, suggesting about 120 m/s (Lognonné et al., 2020). The lower bounds are comparable to those proposed by Lognonné et al. (2020) for similar compliance inversions. In both cases, however, it should be kept in mind that because of the limited bandwidth of the observations (especially towards high frequencies), the measurements are not sensitive to very shallow layers. Moreover, it can be noticed that the a posteriori distribution is asymmetric (Figure 17a), with low values of  $E$  more likely than very high values.

When taking into account the effect of confining stress (M2 inversion, Figure 17c), the  $1\sigma$  interval for  $E$  at the surface is lowered to 12–31 MPa (dust devil convective vortices) and 12–25 MPa (compliance marker), values which are much closer to the pre-landing estimates. These provide  $P$  wave velocities in the range 136–152 m/s for the two median values, slightly higher than the measure based on HP<sup>3</sup>-hammering travel

**Table 3**  
Inversion Results for the Different Dataset and Schemes in Terms of Young Modulus at the Surface and at 20 m Depth

Inversion	Dataset	Depth (m)	Median (MPa)	1 $\sigma$ (MPa)	$V_p$ (m/s)
M1	Dust devil vortices	0 m	100	30-200	304
M1	Compliance marker	0 m	80	30-125	272
M2	Dust devil vortices	0 m	25	12-31	152
M2	Compliance marker	0 m	20	12-25	136
M1	Dust devil vortices	20 m	600	200- 3900	744
M1	Compliance marker	20 m	1000	300-5000	961
M2	Dust devil vortices	20 m	600	300-3900	744
M2	Compliance marker	20 m	600	500-1000	744

Note. See text for explication and caveats. The last column provides the equivalent  $V_p$  for a  $\nu = 0.25$ , a density of  $1,300 \text{ kg/m}^3$ , and the median  $E$ .

times ( $V_p = 120 \text{ m/s}$ ). However, the difference between the M1 and M2 inversions suggests that the inversion scheme has a major impact on the retrieved Young modulus at the surface. We thus recommend to consider these values with the due attention to the inversion procedure.

The Young modulus at 20 m depth (Figures 17b and 17d) has less prominent probability peaks, but the distribution is still significantly different from the prior. Interestingly, in this case, all the inversions produce consistent and similar results (Table 3) with a median value of 0.6–1 GPa fully compatible with a layer of coarse ejecta. This strongly suggests that the observed compliance is sensitive to a relatively stiff layer of rock at some depth and to an integrated value in the regolith layer. However, note that the confidence intervals for  $E$  at depth span one order of magnitude, apart for the M2 inversion of the compliance-marker measurements, for which the a posteriori uncertainty is roughly a factor of 2. In addition, the precise depth is not straightforward to infer: In particular, the depth of 20 m is the one where we put the homogeneous half space in the M1 inversions, and it is in fact representative of what happens below the regolith, not really representative of the elastic properties at exactly 20 m depth.

To estimate the thickness of the regolith layer, we need to focus on the M2 inversion only. Indeed, the M1 inversion does not give a quantitative estimate of this depth since the inversion is performed with several layers; thus, several discontinuities are present in each output model. Therefore, the M1 inversion results (Figures 15c and 15d) can be used just to infer the existence of such a transition based on the bimodal pdf: Avoiding the regions of significant sensitivity close to the surface and close to 20 m depth, the transition can be guessed to lie between 3 and 15 m depth, with the best models showing a sharp discontinuity around 3–4 m depth (geological observations by Warner et al., 2017, fix it between 3 and 12–18 m in the region of the InSight landing site). The M2 inversion, instead, explicitly solves for the thickness of the regolith (Figure 18),

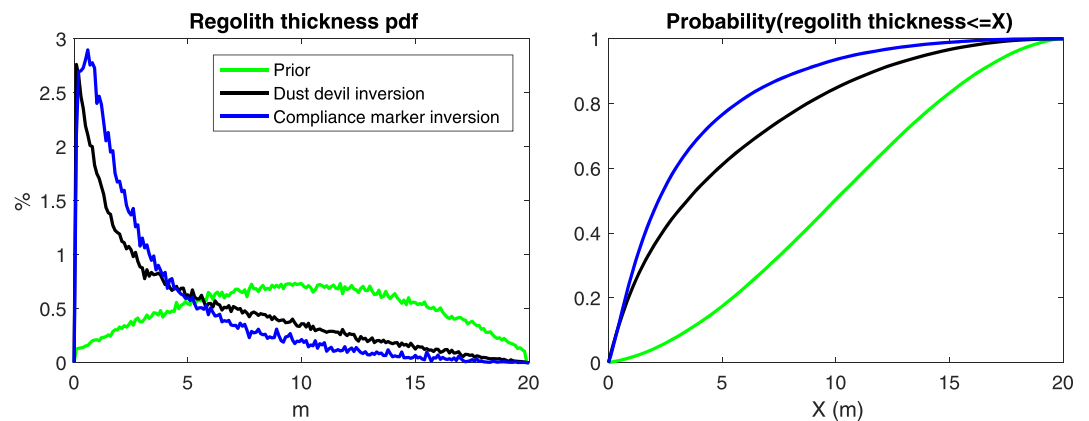


**Figure 18.** Probability of the regolith thickness at the InSight landing site. Left panel: pdf, the green line shows the prior, the black and blue lines the results from the dust devil and the compliance marker inversions, respectively. Right panel: cumulative distribution function.

and in particular, the inversion of dust devil vortex data yields the confidence interval 0.7–8.8 m, whereas the compliance marker inversion suggests a depth of 0.6–5.7 m. Unsurprisingly, the regolith thickness is not precisely retrieved: It is an inherently difficult parameter to find with compliance analysis, as shown both by the nature of the forward problem (Figures 5 and 9) and by the inversion of synthetic datasets (Figure 12). Nevertheless, the compliance observations discussed in this study and the cumulative distribution shown in Figure 18 can be used to test the compatibility and likelihood of any proposed model for the near-surface stratigraphy at the InSight landing site.

## 6. Conclusion

Two different and independent sets of compliance measurements at the InSight landing site from SEIS and APSS data have been inverted. The inversion provides information about the elastic properties in the near surface and more precisely about the Young modulus (the Poisson's ratio being poorly constrained by compliance measurements).

This preliminary inversion shows an increase of the Young modulus by at least one order of magnitude between the regolith at the very surface and stiffer rock (with Young modulus of several hundreds MPa) at some depth, in line with the expected properties of a blocky-ejecta layer observed in the area below the regolith (Golombek et al., 2017). The depth of the transition is not precisely determined, with the probability distribution spread around a median value of about 3 m, which is close to the minimum value inferred from remote-sensing geological observations prior to the InSight landing (Warner et al., 2017). It is also likely that a gradient between regolith and bedrock might be acceptable, and its constraints will be the subject for future analysis. Also, the use of more informed prior covariance structure can provide smoother results by avoiding models with extreme structural discontinuities, and this option will be explored in future works.

Although the uncertainties on the structure are large, our results are among the very first seismic constraining the structure below SEIS and can be used to test the likelihood of proposed models for the near surface. Inclusion of other information, for example, seismic velocities from the HP3-SEIS hammering experiment (Lognonné et al., 2020), may lead to better constraints on the structure, and the design of the MCMC inversion scheme adopted in this study permits to easily include and modify a priori knowledge, as well as to perform joint inversion of different datasets. The ongoing continuous monitoring by SEIS and APSS will also lead to a quality improvement of compliance observations, and selection of individual high-frequency events (see Banerdt et al., 2020, for a first example) may inform about the elastic properties within the surface regolith layer with higher precision.

## References

- Ansan, V., Hauber, E., Golombek, M., Warner, N., Grant, J., Maki, J., et al. (2019). InSight landing site: Stratigraphy of the regolith beneath the lander and in its surroundings, and implications for formation processes. *Lunar and Planetary Science Conference*, 50, 1310.
- Banerdt, W. B., Smrekar, S., Banfield, D., Giardini, D., Golombek, M., Johnson, C., et al. (2020). Initial results from the InSight mission to Mars. *Nature Geoscience*, 13, 183–189.
- Banfield, D., Rodriguez-Manfredi, J. A., Russell, C. T., Rowe, K. M., Leneman, D., Lai, H. R., et al. (2018). InSight auxiliary payload sensor suite (APSS). *Space Science Reviews*, 215(1), 4.
- Banfield, D., Spiga, A., Newman, C., Forget, F., Lemmon, M., Lorenz, R., et al. (2020). The atmosphere of Mars as observed by InSight. *Nature Geoscience*, 13, 190–198.
- Beauduin, R., Lognonné, P., Montagner, J.-P., Cacho, S., Karczewski, J., & Morand, M. (1996). The effects of atmospheric pressure changes on seismic signals or how to improve the quality of a station. *Bulletin of the Seismological Society of America*, 86(6), 1760–1769.
- Bonnefoy-Claudet, S., Kohler, A., Cornou, C., Wathelet, M., & Bard, P.-Y. (2008). Effects of love waves on microtremor H/V ratio. *Bulletin of the Seismological Society of America*, 98(1), 288–300.
- Crawford, W. C., Webb, S. C., & Hildebrand, J. A. (1991). Seafloor compliance observed by long-period pressure and displacement measurements. *Journal of Geophysical Research*, 96(B10), 16,151–16,160.
- Delage, P., Karakostas, F., Dhemaied, A., Belmokhtar, M., Lognonné, P., Golombek, M., et al. (2017). An investigation of the mechanical properties of some Martian regolith simulants with respect to the surface properties at the InSight mission landing site. *Space Science Reviews*, 211(1), 191–213.
- Doran, A. K., & Laske, G. (2019). Seismic structure of marine sediments and upper oceanic crust surrounding Hawaii. *Journal of Geophysical Research: Solid Earth*, 124, 2038–2056. <https://doi.org/10.1029/2018JB016548>
- Drilleau, M., Beucler, É., Mocquet, A., Verhoeven, O., Moebs, G., Burgos, G., et al. (2013). A Bayesian approach to infer radial models of temperature and anisotropy in the transition zone from surface wave dispersion curves. *Geophysical Journal International*, 195(2), 1165–1183.
- Folkner, W. M., Dehant, V., Le Maistre, S., Yseboodt, M., Rivoldini, A., Van Hoolst, T., et al. (2018). The rotation and interior structure experiment on the InSight mission to Mars. *Space Science Reviews*, 214(5), 100.
- García, R. G., Kenda, B., Kawamura, T., Spiga, A., Murdoch, P., Widmer-Schnidrig, R., et al. (2020). Pressure effects on SEIS-INSIGHT instrument, improvement of seismic records and characterization of long period atmospheric waves from ground displacements. *Journal of Geophysical Research*, press. <https://doi.org/10.1029/2019JE006278>

## Acknowledgments

The data from the InSight mission used in this study were retrieved through InSight Mars SEIS data Service (2020). We acknowledge NASA, CNES, partner agencies and Institutions (UKSA, SSO, DLR; JPL, IGGP-CNRS, ETHZ, IC, MPS-MPG) and the operators of JPL, SISMOC, MSDS, IRIS-DMC, and PDS for providing SEED SEIS data. Modeling and derived data used to produce figures and tables and to drive our interpretations are available at <https://doi.org/10.5281/zenodo.3738380>. M1 and M2 models computation used HPC resources of CINES under the allocation A0050407341 and A0070407341 attributed by GENCI (Grand Equipement National de Calcul Intensif). French authors acknowledge the French Space Agency for supporting both operation and science analysis. Additional support was provided by ANR (ANR-14-CE36-0012-02 and ANR-19-CE31-0008-08) and for IGGP team by UnivEarthS Labex program (ANR-10-LABX-0023), IDEX Sorbonne Paris Cité (ANR-11-IDEX-0005-0). The US authors were supported by the InSight Project at the Jet Propulsion Laboratory, under a contract with NASA. This is IGGP Contribution Number 4123. This is InSight Contribution Number 111. We gratefully thank the Editor, an anonymous reviewer and Rick Aster, whose comments helped us improving the manuscript.

- Golombek, M., Grott, M., Kargl, G., Andrade, J., Marshall, J., Warner, N., et al. (2018). Geology and physical properties investigation by the InSight lander. *Space Science Reviews*, 214, 84.
- Golombek, M., Kipp, D., Warner, N., Daubar, I. J., Ferguson, R., Kirk, R. L., et al. (2017). Selection of the InSight landing site. *Space Science Reviews*, 211(1), 5–95.
- Golombek, M., Warner, N., Grant, J., Hauber, E., Ansan, V., Weitz, C. M., et al. (2020). Geology of the InSight landing site on Mars. *Nature Communications*, 11.
- Haskell, N. A. (1953). The dispersion of surface waves on multilayered media. *Bulletin of the Seismological Society of America*, 43(1), 17–34.
- Hastings, W. K. (1970). Monte carlo sampling methods using Markov chains and their applications. *Biometrika*, 57, 97–109.
- InSight Mars SEIS data Service (2020). SEIS raw data, InSight mission. IPGP, JPL, CNES, ETHZ, ICL, MPS, ISAE-Supaero, LPG, MSFC.
- Kenda, B., Lognonné, P., Spiga, A., Kawamura, T., Kedar, S., Banerdt, W. B., et al. (2017). Modeling of ground deformation and shallow surface waves generated by Martian dust devils and perspectives for near-surface structure inversion. *Space Science Reviews*, 211(1), 501–524.
- Kobayashi, N., & Nishida, K. (1998). Continuous excitation of planetary free oscillations by atmospheric disturbances. *Nature*, 395, 357–360.
- Kwong, R. H., & Johnston, E. W. (1992). A variable step size LMS algorithm. *IEEE Transactions on Signal Processing*, 40(7), 1633–1642.
- Lognonné, P., & Mosser, B. (1993). Planetary seismology. *Surveys in Geophysics*, 14(3), 239–302.
- Lognonné, P., Banerdt, W. B., Giardini, D., Pike, W. T., Christensen, U., Laudet, P., et al. (2019). SEIS: Insight's seismic experiment for internal structure of Mars. *Space Science Reviews*, 215(1), 12.
- Lognonné, P., Banerdt, W. B., Pike, W. T., Giardini, D., Christensen, U., Garcia, R. F., et al. (2020). Constraints on the shallow elastic and anelastic structure of Mars from InSight seismic data. *Nature Geoscience*, 13, 213–220.
- Metropolis, N., Rosenbluth, A. W., Rosenbluth, M. N., Teller, A. H., & Teller, E. (1953). Equation of state calculations by fast computing machines. *Journal of Chemical Physics*, 21, 1087–1091.
- Mimoun, D., Murdoch, N., Lognonné, P., Hurst, K., Pike, W. T., Hurley, J., et al. (2017). The noise model of the SEIS seismometer of the InSight mission to Mars. *Space Science Reviews*, 211(1), 383–428.
- Morgan, P., Grott, M., Knapmeyer-Endrun, B., Golombek, M., Delage, P., Lognonné, P., et al. (2018). A pre-landing assessment of regolith properties at the InSight landing site. *Space Science Reviews*, 214(6), 104.
- Mosegaard, K. (1998). Resolution analysis of general inverse problems through inverse Monte-Carlo sampling. *Inverse Problems*, 14, 405–426.
- Mosegaard, K., & Tarantola, A. (1995). Monte-Carlo sampling of solutions to inverse problems. *Journal of Geophysical Research*, 100, 12,431–12,447.
- Murdoch, N., Kenda, B., Kawamura, T., Spiga, A., Lognonné, P., Mimoun, D., & Banerdt, W. B. (2017). Estimations of the seismic pressure noise on Mars determined from large eddy simulations and demonstration of pressure decorrelation techniques for the InSight mission. *Space Science Reviews*, 211(1), 457–483.
- Nakamura, Y. (1989). A method for dynamic characteristics estimation of subsurface using microtremor on the ground surface. *Railway Technical Research Institute, Quarterly Reports*, 30(1), 25–33.
- Nishikawa, Y., Lognonné, P., Kawamura, T., Spiga, A., Stutzmann, E., Schimmel, M., et al. (2019). Mars' Background Free Oscillations. *Space Science Reviews*, 215. <https://doi.org/10.1007/s11214-019-0579-9>
- Panning, M. P., Beucler, E., Drilleau, M., Mocquet, A., Lognonné, P., & Banerdt, W. B. (2015). Verifying single-station seismic approaches using Earth-based data: Preparation for data return from the InSight mission to Mars. *Icarus*, 248, 230–242.
- Panning, M. P., Lognonné, P., Bruce Banerdt, W., Garcia, R., Golombek, M., Kedar, S., et al. (2017). Planned products of the Mars structure service for the InSight mission to Mars. *Space Science Reviews*, 211(1), 611–650.
- Savoie, D., Richard, A., Goutaudier, M., Onufer, N. P., Wallace, M. C., Mimoun, D., et al. (2019). Determining true north on Mars by using a sundial on InSight. *Space Science Reviews*, 215, 2.
- Shapiro, N. M., & Campillo, M. (2004). Emergence of broadband Rayleigh waves from correlations of the ambient seismic noise. *Geophysical Research Letters*, 31(7).
- Sorrells, G. G. (1971). A preliminary investigation into the relationship between long-period seismic noise and local fluctuations in the atmospheric pressure field. *Geophysical Journal International*, 26(1-4), 71–82.
- Sorrells, G. G., McDonald, J. A., Der, Z. A., & Herrin, E. (1971). Earth motion caused by local atmospheric pressure changes. *Geophysical Journal International*, 26(1-4), 83–98.
- Spohn, T., Grott, M., Smrekar, S. E., Knollenberg, J., Hudson, T. L., Krause, C., et al. (2018). The heat flow and physical properties package (HP3) for the InSight mission. *Space Science Reviews*, 214(5), 96.
- Spiga, A., Banfield, D., Teanby, N. A., Forget, F., Lucas, A., Kenda, B., et al. (2018). Atmospheric science with InSight. *Space Science Reviews*, 214(7), 109.
- Tanimoto, T., Heki, K., & Artru-Lambin (2015). 4.16 - Interaction of Solid Earth, Atmosphere and Ionosphere. In G. Schubert (Ed.), *Treatise on Geophysics* (2nd ed., pp. 421–443). Oxford: Elsevier. <https://doi.org/10.1016/B978-0-444-53802-4.00083-X>
- Tanimoto, T., & Wang, J. (2018). Low-frequency seismic noise characteristics from the analysis of co-located seismic and pressure data. *Journal of Geophysical Research: Solid Earth*, 123, 5853–5885. <https://doi.org/10.1029/2018JB015519>
- Tanimoto, T., & Wang, J. (2019). Theory for deriving shallow elasticity structure from collocated seismic and pressure data. *Journal of Geophysical Research: Solid Earth*, 124, 5811–5835. <https://doi.org/10.1029/2018JB017132>
- Thomson, W. T. (1950). Transmission of elastic waves through a stratified solid medium. *Journal of Applied Physics*, 21, 89–93.
- Tibuleac, I. M., & von Seggern, D. (2012). Crust-mantle boundary reflectors in Nevada from ambient seismic noise autocorrelations. *Geophysical Journal International*, 189(1), 493–500.
- Warner, N. H., Golombek, M., Grant, J., Wilson, S., Hauber, E., Ansan, V., et al. (2019). Geomorphology and origin of Homestead hollow, the landing location of InSight on Mars. In *Lunar and Planetary Science Conference*, 50, pp. 1310.
- Warner, N. H., Golombek, M. P., Sweeney, J., Ferguson, R., Kirk, R., & Schwartz, C. (2017). Near surface stratigraphy and regolith production in southwestern Elysium Planitia, Mars: Implications for Hesperian-Amazonian terrains and the InSight lander mission. *Space Science Reviews*, 211(1), 147–190.
- Withers, M. M., Aster, R. C., Young, C. J., & Chael, E. P. (1996). High-frequency analysis of seismic background noise as a function of wind speed and shallow depth. *Bulletin of the Seismological Society of America*, 86(5), 1507–1515.
- Zha, Y., & Webb, S. C. (2016). Crustal shear velocity structure in the Southern Lau Basin constrained by seafloor compliance. *Journal of Geophysical Research: Solid Earth*, 121, 3220–3237. <https://doi.org/10.1002/2015JB012688>
- Zürn, W., Exß, J., Steffen, H., Kroner, C., Jahr, T., & Westerhaus, M. (2007). On reduction of long-period horizontal seismic noise using local barometric pressure. *Geophysical Journal International*, 171, 780–796.

- Zürn, W., & Widmer, R. (1995). On noise reduction in vertical seismic records below 2 mHz using local barometric pressure. *Geophysical Research Letters*, *22*(24), 3537–3540.
- Zürn, W., & Wielandt, E. (2007). On the minimum of vertical seismic noise near 3 mHz. *Geophysical Journal International*, *168*(2), 647–658.